
Article:
Epton, Ryan G., Unsworth, William P. orcid.org/0000-0002-9169-5156 and Lynam, Jason M. orcid.org/0000-0003-0103-9479 (2022) DFT Studies of Au(I) Catalysed Reactions : Anion Effects and Reaction Selectivity. Israel Journal of Chemistry. e202200033. ISSN 0021-2148

https://doi.org/10.1002/ijch.202200033

Review

Israel Journal of Chemistry
www.ijc.wiley-vch.de

doi.org/10.1002/ijch.202200033

DFT Studies of Au(I) Catalysed Reactions: Anion Effects and Reaction Selectivity

Ryan G. Epton,*[a] William P. Unsworth,[a] and Jason M. Lynam*[a]

Abstract: Density functional theory (DFT) is a powerful tool that can aid in the exploration and development of synthetic chemistry, and its use is often applied in the chemistry of gold(I) catalysis. In this review, we discuss two different facets of these calculations – namely, the exploration and explanation of anion effects, and the regioselectivity and speciation of gold(I)-catalysed reactions. The research described herein clearly shows the importance of including the anion in DFT studies of Au(I)-catalysed reactions, especially when using low polarity solvents, or where hydrogen-bonding is prevalent. Additionally, we show that whilst using DFT to study the selectivity of reactions can be successful, benchmarking the computational results against experimental data is vitally important for ensuring that the model is accurately describing the observed results.

Keywords: catalysis · gold · DFT · anion effects · π-acids

1. Introduction

Interest in gold catalysis has increased exponentially over the last 20 years.[1] Primarily, the catalytic applications of gold(I) are based on its ability to act as a π-acid. Au(I) complexes are able to coordinate to and activate unsaturated C–C bonds, particularly alkynes,[2] although similar reactivity has also been observed with alkenes[3] and allenes.[4] The typical mechanism proposed for gold(I)-catalysed reactions involves the coordination of the gold(I) complex to the unsaturated C–C bond, forming an $\eta^2(\pi)$ complex, which activates the π-system to undergo attack by a nucleophile (**1**→**2**). Protiodemetallation then occurs (**2**→**3**), regenerating the Au(I) catalyst and allowing further reactions to take place (Figure 1).[5]

The nature of the gold catalyst used, and its coordination environment, can have a significant effect on reaction outcomes. This may be by simply increasing the reaction yield, but in many cases, it can also alter the reaction selectivity and change the ratio of products that are formed. The ligand used can also influence the reaction outcomes, with phosphine or *N*-heterocyclic carbene (NHC) ligands being the most common, and the counterion used is also often altered during reaction optimisation.[6]

Computational chemistry utilising density functional theory (DFT) is frequently used in studies of catalytic reactions.[7] DFT offers a good balance of calculation time versus accuracy and is, therefore, often the method of choice to explore the mechanism of transition metal catalysed reactions.

Papers benchmarking the success of DFT calculations to study gold(I) complexes have been published, which provide recommendations on the level of theory best employed for studying reactions using gold(I) catalysis.[8] The double-hybrid B2PLYP functional performed well across multiple studies, with BP86,[8b,d] PBE0,[8c] wB97X[8c] and M06[8a,b] functionals also shown to be successful at modelling the energies and geometries of gold(I) complexes. Ahlrichs' def2 basis sets generally performed well, with a triple-ζ type basis set with polarisation recommended.[8d] Electrostatic core potentials (ECPs) such as LANL2DZ or SDD are commonly used on the gold atom to account for relativistic effects.

In this review paper, we highlight potential considerations when using DFT to explore gold(I) catalysis. Recent examples of the use of DFT to explore reaction processes are provided, focussing on the effects of including the anions used in the reaction, and studying how DFT can be used to explore the selectivity of gold(I)-catalysed reactions. With a wide range of literature available, it was not possible to review them all, however other papers which were instructive are highlighted.[9]

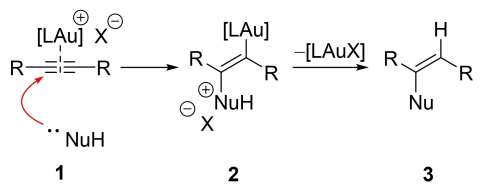

Figure 1. Typical scheme for alkyne activation by gold(I) cations.

[a] *R. G. Epton, Dr. W. P. Unsworth, Dr. J. M. Lynam*
Department of Chemistry, University of York
Heslington, York, YO10 5DD (UK)
E-mail: rge500@york.ac.uk
jason.lynam@york.ac.uk

Note, throughout this review, we use numbers to indicate compounds, whereas DFT calculated states are denoted by letters.

2. Using DFT to Explain the Effects of the Anion on the Reaction Mechanism

In reactions utilising gold(I) catalysts, typically a ligated gold(I) chloride (LAuCl) precatalyst is used, which is then activated by a metal salt containing a weakly coordinating anion. This results in salt metathesis, enabling the formation of an active Lewis acidic cationic gold(I) species (LAu^+) in solution which is catalytically active.[10] Other activation methods, such as protonolysis of an alkylgold and hydroxide species,[11] or via sonication and centrifugation,[12] have been used to avoid any competing "silver effects".[12,13]

Many studies utilising DFT methods have successfully captured the experimental reaction outcomes by focussing solely on the cationic gold-based component of the catalyst system without consideration of the counteranion.[14] However, recent papers have detailed instances where optimising the counterion has been important for the course of the reaction.[6,15]

In 2009, Tarantelli, Macchioni and co-workers studied ion pairing in cationic olefin-gold(I) complexes.[16] Two 4-Me-styryl gold(I) complexes were synthesised with either a triphenylphosphine (**4PPh$_3$**) or NHC ligand (**4NHC**, NHC = 1,3-bis(di-*iso*-propylphenyl)-imidazol-2-ylidene) (Figure 2). Both complexes had a tetrafluoroborate anion which enabled the use of ^{19}F,^{1}H-HOESY NMR experiments to study the preferred orientation of the anion with respect to the gold complex under low temperature conditions.

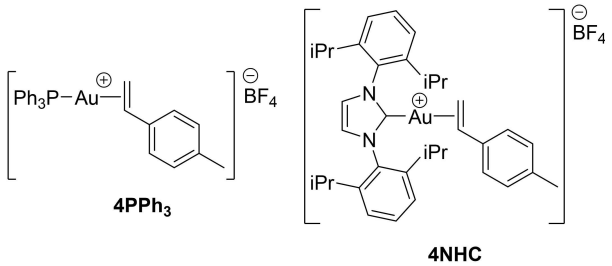

Figure 2. 4-Me-styrlyl gold(I) complexes studied by Zuccaccia *et al.*[16]

These NMR studies showed that the choice of ligand influenced the ion-pairing (Figure 3), with strong contacts observed between the olefinic protons and the tetrafluoroborate anion in complex **4PPh$_3$**. In contrast, for complex **4NHC**, contacts were observed primarily with the imidazole protons furthest away from the styrene.

The observed NMR data were further supported by DFT calculations. Geometry optimisations (at the BLYP/ZORA/TZ2P level of theory) of varying configurations were performed, and these confirmed that the lowest energy arrangement of the complexes agreed with the NMR experiments (Figure 4).

This effect was rationalised by analysing the charge distribution and the Coulomb potential of both the styrene cationic complexes (Figure 5). The olefinic protons of the coordinated styrene and, in the case of complex **4NHC**, the imidazolium protons at the back of the complex were shown to have the greatest positive charge within the complex (denoted as a blue colour on the isodensity surface), and therefore be the most attractive points for counterion coordination.

Further studies examined the effects of changing both the ligand and the unsaturated hydrocarbon coordinated to the

Ryan G. Epton received his Masters' degree in 2018 at the University of Leicester, completing his Masters' research project under the supervision of Dr Sandeep Handa. Ryan then joined the University of York under the joint supervision of Dr William P Unsworth and Dr Jason M Lynam, where he is now in the final year of his Ph.D. studies. His current research interests are in the use of computational chemistry in organic synthesis and transition metal catalysis.

William P. Unsworth is a Senior Lecturer in Organic Chemistry at the University of York. His group's research interests include ring expansion approaches for the synthesis of medium-sized rings and macrocycles and the development of new catalytic methods, using metal-based catalysts, photochemical activation and biocatalysis. He has published over 60 peer reviewed papers to date won the RSC Hickinbottom Award for his work on the synthesis of spirocycles and macrocycles.

Jason M. Lynam is a Reader in Inorganic Chemistry at the University of York. His group's research interests are focussed on mechansitic aspects of organometallic chemistry. This includes the application of computational chemistry and time-resolved spectroscopy to the study of metal-catalysed reactions. He has published over 110 peer reviewed papers and was a principal investigator in the team that was awarded the 2021 RSC Horizon Prize in Physical Organic Chemistry for work on unveiling the mechanistic steps in Mn-catalysed reactions.

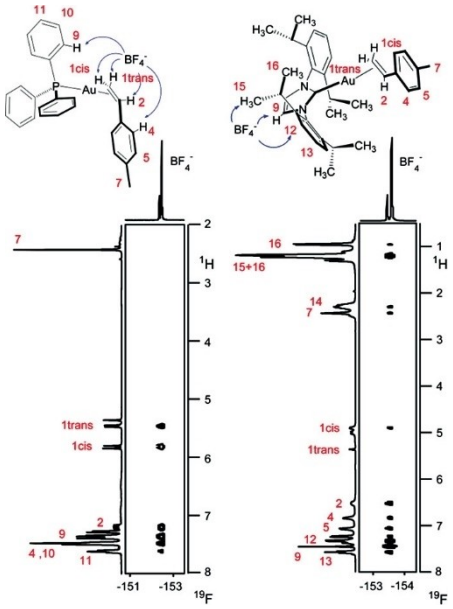

Figure 3. Low temperature $^{19}F,^{1}H$-HOESY spectra of **4PPh$_3$** (left) and **4NHC** (right). Key ion-pairing contacts have been highlighted with assignments made by Zuccaccia *et al.* Reprinted with permission from ref [16]. Copyright 2009 American Chemical Society.

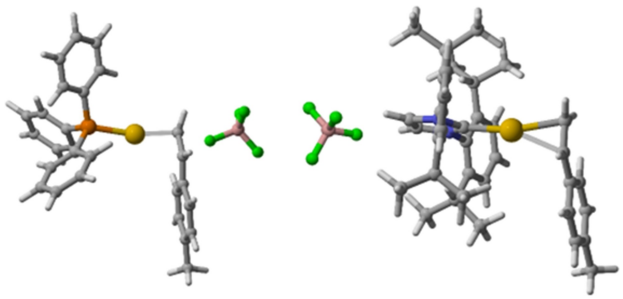

Figure 4. Lowest energy arrangements of **4PPh$_3$** (left) and **4NHC** (right) as calculated by DFT by Zuccaccia *et al.*, calculated at the BLYP/ZORA/TZ2P level of theory. Structures reproduced using coordinates located in the original paper's ESI.

gold(I) cation, which highlighted that the anion coordination depends greatly on the ligands in the cationic unit, with coordination most likely observed around the most acidic protons, rather than the gold centre.[17–19]

This body of work has demonstrated that the location of the anion with respect to the catalytically active cation can be predicted and is often near the most positively charged sites within the complex, providing a starting point for other researchers to consider when including the counterion in their DFT calculations.

In 2021, an extensive report by Sorbelli *et al.* on the gold(I)-catalysed Meyer-Schuster rearrangement of 1-phenyl-2-propyn-1-ol **5** was published, particularly focused upon the effects of both the solvent and the counteranion on the

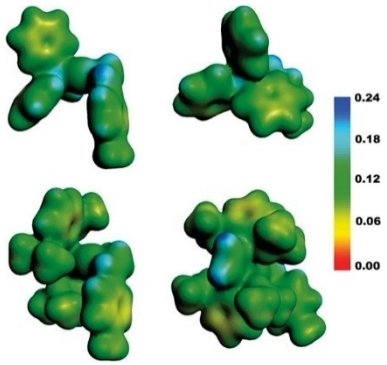

Figure 5. Side (left) and back (right) views of the DFT calculated structures of **4PPh$_3$** (top) and **4NHC** (bottom), without counterion. Coulomb potential is mapped on an electronic isodensity surface ($\rho = 0.007$ e/Å^3. Coulomb potential in au). Reprinted with permission from ref [16]. Copyright 2009 American Chemical Society.

turnover frequency (TOF) of the reaction.[20] Experimentally, clear trends were found in the turnover frequency (TOF) of the reaction, with the efficiency of the reaction decreasing with increasing polarity of the solvent, and the specific counterion used ($TfO^- > TsO^- > BF_4^- > TFA^-$). Selected optimisation results are shown in Table 1.

The authors used DFT studies to rationalise these data. Formation of $\eta^2(\pi)$-alkyne complex **B** from the uncoordinated species (**5** and **7**) was considered. Intermediates involved during de-coordination of the counterion demonstrated that the anion interacts with both the gold atom and the hydrogen of the terminal alkyne (Figure 6).

Whereas both the tosylate and triflate anions (X^-=TsO^- and TfO^-, Figure 6) were predicted to be able to form complex

Table 1. NHCAuX catalysed Meyer-Schuster rearrangement of 1-phenyl-2-propyn-1-ol **5** to cinnamaldehyde **6** at 50 °C.

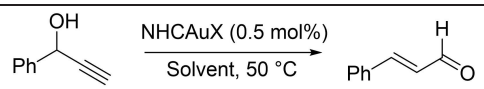

5 **6**

Entry	Solvent	Catalytic System[a]	Conv.[b]/%	TOF[c]/h^{-1}
1	*p*-Cymene	NHCAuOTf	91	394
2	*p*-Cymene	NHCAuCl/AgOTs[d]	11	44
3	*p*-Cymene	NHCAuCl/AgTFA[d]	0.4	2
4	*p*-Cymene	NHCAuCl/AgBF$_4$[d]	7	28
5	*p*-Cymene	NHCAuCl/AgOTf[d]	30	115
6	γ-Valerolactone	NHCAuOTf	23	105

[a] NHCAuOTf (0.0025 mmol), **5** (0.5 mmol), solvent (200 μL). [b] Determined by the average value of three measurements after 30 minutes by ^{1}H NMR. [c] TOF = ($mol_{product}/mol_{catalyst}$)/*t* calculated after 30 minutes. [d] 1.1 eq of silver salt used. NHC = 1,3-bis(di-*iso*-propylphenyl)-imidazol-2-ylidene

Israel Journal of Chemistry

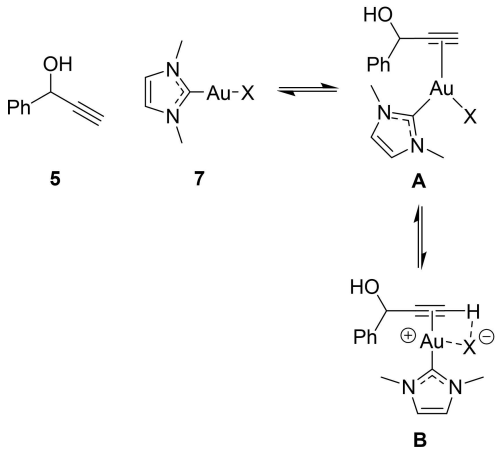

Figure 6. Proposed intermediate structures calculated for the formation of $\eta^2(\pi)$-alkyne complex **B** from the uncoordinated species **5** and **7**.

B, a low-lying transition state (+4.2 kcal mol^{-1} from **5** and **7** at the BP86/ZORA//B2PLYP/CPCM level of theory) was found when trifluoroacetate was calculated as the anion (X=TFA, Figure 6), in which the alkyne was deprotonated, resulting in σ-bonded gold alkynyl complex **8** (Figure 7). It was postulated that this was the reason behind the poorest efficiency observed in the experiments using AgTFA as the co-catalyst.

The proposed mechanism for the Meyer-Schuster rearrangement, and the intermediates studied, are shown in Figure 8. To explain the difference in reactivity when using the other anions (namely OTf$^-$, OTs$^-$ and BF_4^-), the energies of the proposed transition states and intermediates involved in

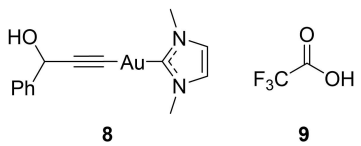

Figure 7. σ-Bonded gold alkynyl complex **8** with the formation of acid **9**, calculated by DFT when trifluoroacetate was the counterion.

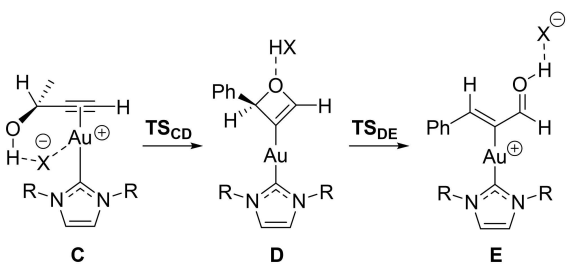

Figure 8. Intermediates studied in the Meyer-Schuster rearrangement of **5**. X=OTs, OTf or BF_4. A simplified NHC was used in the calculations (R=Me).

the catalytic cycle were calculated (BP86/ZORA/D3//B2PLYP/CPCM), with the anion proposed to coordinate to the alcohol of the starting material. The authors found that the first transition state ($\mathbf{TS_{CD}}$), corresponding to attack of the alcohol into the gold-coordinated alkyne, was the highest energy, and the relative energies for the three counterions were consistent with the experimental data, in which the triflate was fastest (+32.6 kcal mol^{-1} relative to **C**), followed by the tosylate (+34.3 kcal mol^{-1}) and then the tetrafluoroborate (+36.9 kcal mol^{-1}). The authors proposed that the main factors in the energy of transition state ($\mathbf{TS_{CD}}$) were the hydrogen-accepting ability of the anion, and how well the anion coordinates to the gold atom.

Finally, the effect of solvent polarity was also considered. In low polarity media it is understood that an ion pair is formed due to the solvent's inability to strongly coordinate the cation and anion. In more polar solvents, solvation of the cation and anion is efficient, separating the ions.[21] This effect was studied by explicitly modelling a molecule of γ-valerolactone to coordinate to the alcohol. Whilst a structure for the equivalent oxetene intermediate (**D**, Figure 8) couldn't be found, the transition state for a one-step process was calculated (**F**, Figure 9) which showed a higher energy than the triflate-assisted process (+33.4 vs +31.6 kcal mol^{-1} in the gas phase at the BP86/ZORA/D3//B2PLYP level of theory), which is consistent with the experimental observations.

Overall, the study demonstrates how DFT enables the rationalisation of the reaction rates with different anions, in both the formation of the active catalytic species, and then also in the key intramolecular cyclisation step of the catalytic cycle. Insight from computational chemistry was also able to rationalise the solvent effects, in that higher polarity solvents restrict the ability for the anion to participate, with higher energy transition states observed.

In 2021, Hussein and co-workers described the impact of different ring-sized NHC ligands on the gold(I)-catalysed cyclisation of propargylic amide **10** to give methylene-3-oxazoline **11** (Figure 10a).[22] As part of this work, DFT was used to study the mechanism of the reaction, to address the role of the counterion in the reaction. It was proposed that the

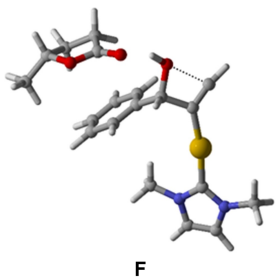

Figure 9. DFT-calculated transition state structure for the Meyer-Schuster rearrangement, in which γ-valerolactone is modelled coordinating to the hydroxyl group. Structures reproduced using coordinates located in the original paper's ESI.

Israel Journal of Chemistry

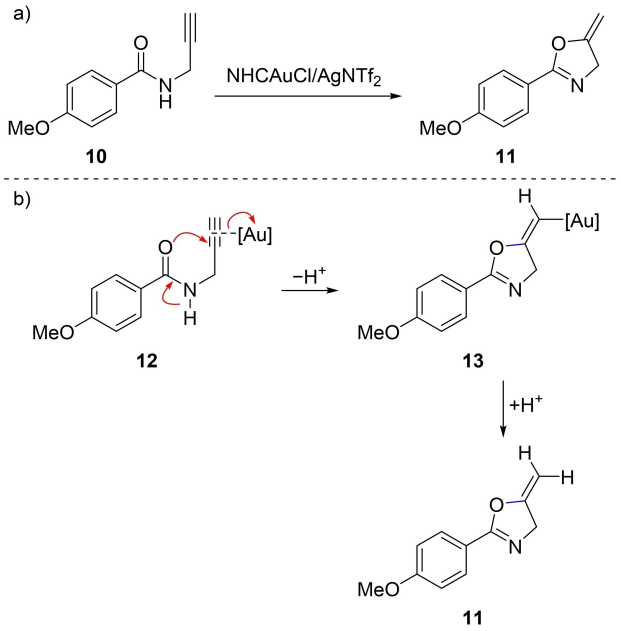

Figure 10. a) Reaction studied by Ma et al.,[22] the cyclisation of propargylic amide **10**, resulting in methylene-3-oxazoline **11**, first reported by Hashmi *et al.* and then used as a standard reaction when comparing different NHC ligands.[22,23] b) Mechanism proposed by Hashmi *et al.* for the formation of **11**.[23]

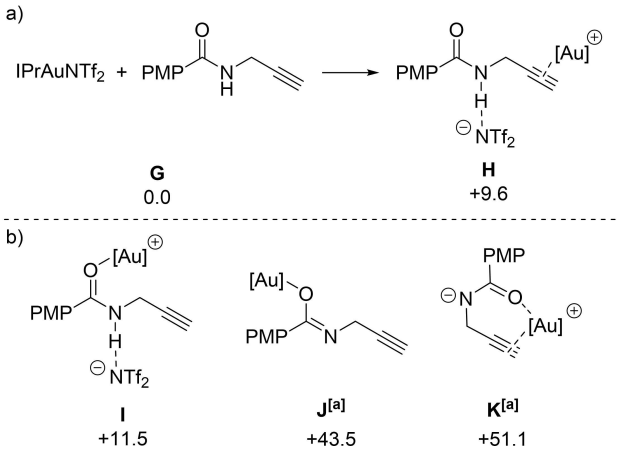

Figure 11. DFT-calculated structures at the SMD($CHCl_3$)-PBE0-D3BJ/def2-TZVP,6-311+G(d,p)//PBE0-D3BJ/SDD,6-31G(d) level of theory. Energies are Gibbs energies in kcal mol^{-1}. [Au]=IPrAu$^+$. a) Preferred configuration of gold(I)-coordination to **10**. b) Other calculated configurations of higher energy. [a] States resulting from loss of $HNTf_2$ from **I**.

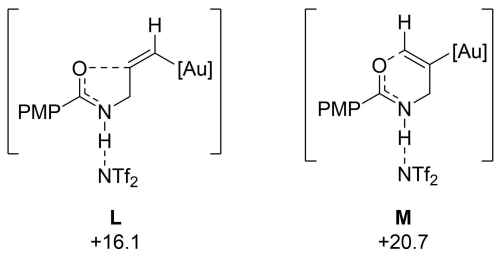

Figure 12. DFT-calculated energies for the transition states of 5-*exo-dig* (**L**) and 6-*endo-dig* (**M**) cyclisations of **H**. Energies are Gibbs energies at the SMD($CHCl_3$)-PBE0-D3BJ/def2-TZVP,6-311+G(d,p)//PBE0-D3BJ/SDD,6-31G(d) level of theory in kcal mol^{-1} with **G** as the reference point. [Au]=IPrAu$^+$. PMP=*p*-methoxyphenhyl.

reaction occurs via nucleophilic attack of the amide carbonyl, aided by the lone pair of the adjacent nitrogen (Figure 10b).[23]

The authors first considered different coordination binding modes, both with and without the anion. The $\eta^2(\pi)$ alkyne gold(I) complex with hydrogen bonding of the triflimide anion (**H**, Figure 11a) was found to be the lowest energy bound complex at +9.6 kcal mol^{-1} energy higher than the separate species at the SMD($CHCl_3$)-PBE0-D3BJ/def2-TZVP,6-311+G(d,p)//PBE0-D3BJ/SDD,6-31G(d) level of theory. Other coordination modes were studied, including *O*-coordinated gold species, with (**I**, Figure 11b) and without deprotonation of the amide nitrogen (**J** and **K**, Figure 11b), however these complexes were much higher in energy.

Considering again the gold(I) alkyne complex with hydrogen bonding anion (**H**), transition states for the possible cyclisations were found (Figure 12). 5-*exo-dig* cyclisation (**L**) was calculated to be energetically preferred over 6-*endo-dig* cyclisation (**M**) by 4.6 kcal mol^{-1} (+16.1 vs +20.7 kcal mol^{-1}), which was consistent with the experimentally observed outcome.

When gold(I)-coordination was considered without the anion, the energy of the intermediate was greatly increased at +16.7 kcal mol^{-1} (**N**, Figure 13). Transition states for the cyclisation of **N** were; however, higher in energy than the equivalent triflimide-coordinated transition states, at +25.5 and +27.2 kcal mol^{-1} for the 5-*exo*- (**O**) and 6-*endo-dig* (**P**) cyclisations respectively, strongly suggesting that the triflimide anion does indeed play an active role in the reaction.

Whilst the cyclised oxazoline intermediate (**Q**, Figure 14a) is calculated to be lower in energy than **H**, the calculated energies when neutral triflimide has dissociated (**R**) are significantly higher at +19 kcal mol^{-1}, prompting further DFT studies on the possible proton-migration processes.

Following reports that water clusters can aid in proton transfer,[24] the possibility of a water-assisted mechanism was considered for the protiodemetallation, however, the calculations predicted this to be higher in energy. Generation of the protonated product **T** and vinyl-gold species **S** by participation of the basic nitrogen of oxazole ring in the product was therefore also considered (Figure 15). Transition state $\mathbf{TS_{QS}}$ (+10.4 kcal mol^{-1}) was found at a much lower energy than the triflimide-promoted pathway. The transition state of protiodemetallation was then calculated as $\mathbf{TS_{S11}}$ (+13.7 kcal mol^{-1}) resulting in two units of the product **11**. Overall, this process was calculated to be lower in energy than the equivalent triflimide anion-assisted process, with the rate-limiting step

Israel Journal of Chemistry

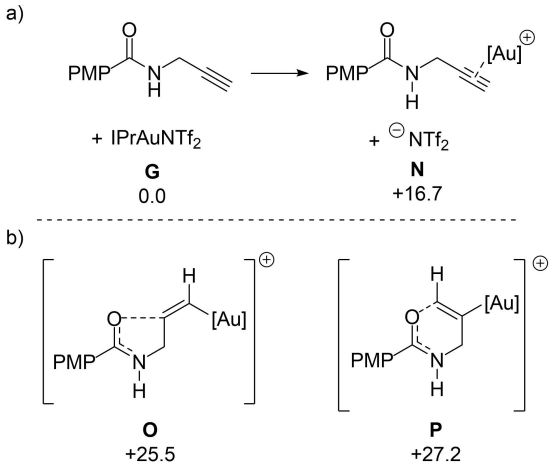

Figure 13. DFT-calculated structures at the SMD($CHCl_3$)–PBE0-D3BJ/def2-TZVP,6-311+G(d,p)//PBE0-D3BJ/SDD,6-31G(d) level of theory. Energies are Gibbs energies in kcal mol^{-1}. [Au]=IPrAu$^+$. a) Ion-separated-coordination of Au(I) to **10**. b) Transition states energies of 5-*exo-dig* (**O**) and 6-*endo-dig* (**P**) cyclisations of **N**.

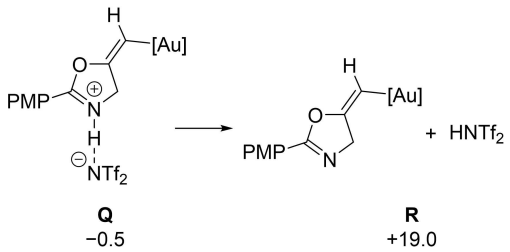

Figure 14. DFT-calculated structures at the SMD($CHCl_3$)-PBE0-D3BJ/def2-TZVP,6-311+G(d,p)//PBE0-D3BJ/SDD,6-31G(d) level of theory. Energies are Gibbs energies in kcal mol^{-1}. [Au]=IPrAu$^+$. Energies of the intermediate gold(I)-oxazoline species, before and after the removal of triflimide.

predicted to be the initial cyclisation (**L**) at 16.1 kcal mol^{-1} in energy.

The DFT data enabled a catalytic cycle to be proposed (Figure 16). First, an initiation cycle, in which cyclisation occurs via a 5-*exo-dig* cyclisation (**L**) promoted by initial coordination of the gold(I) NHC complex to propargylic amide **10**, with hydrogen bonding of the triflimide anion to the amide nitrogen (**H**). A triflimide-assisted proton-migration then occurs resulting in the product (**11**). After initiation, an iterative cycle is predicted to take place, where the oxazole product (**11**) deprotonates intermediate **Q**: this was calculated to be a lower energy pathway than deprotonation by $^-NTf_2$.

The authors demonstrated that coordination of the anion can be important when discussing reaction mechanisms, potentially changing the viability of a predicted mechanism. In this reaction the product itself is predicted to take part in the catalysis. Product participation in this manner could have a pronounced effect on the observed kinetics, and without

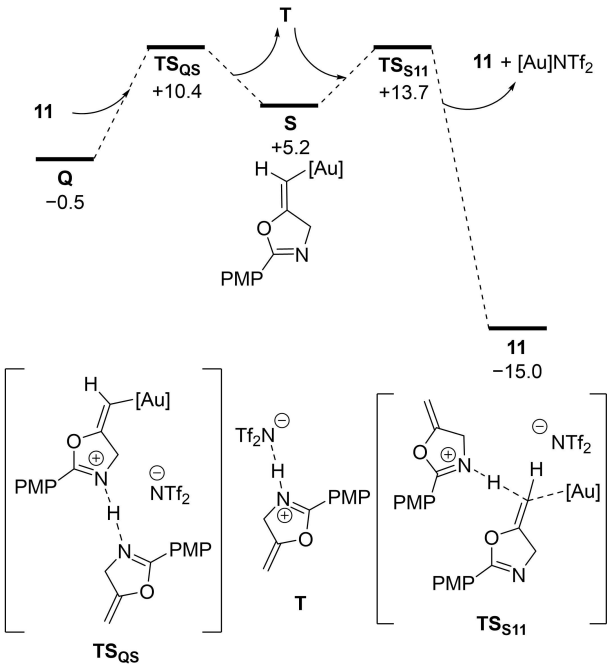

Figure 15. DFT-calculated pathway for oxazoline-assisted proton-migration of **Q**. Energies are Gibbs energies at the SMD(CHCl3)–PBE0-D3BJ/def2-TZVP,6-311+G(d,p)//PBE0-D3BJ/SDD,6-31G(d) level of theory in kcal mol^{-1}. [Au]=IPrAu$^+$.

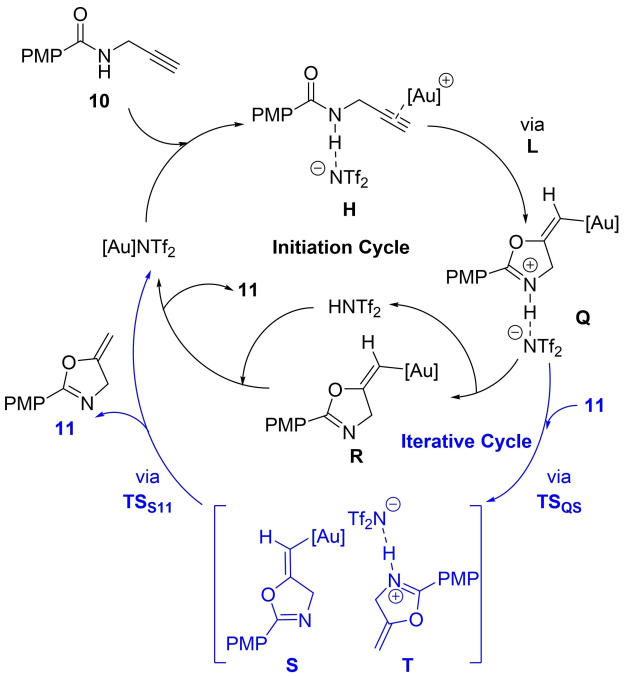

Figure 16. Catalytic cycle proposed by Ma *et al.* for propargylic amide cyclisation. The anion plays a role in the reaction process throughout. Reproduced with permission from ref [22]. Copyright 2022 Royal Society of Chemistry.

considering the anion effects, the rationale for this could be missed.

The handful of papers discussed here only shows a small subset of the studies within the field of gold(I) chemistry where anion effects have been studied by computational chemistry. It is hoped that highlighting these recent examples brings to light the importance of considering the anion when beginning to study a process theoretically. Ligand, substrate, anion, and solvent all should be considered, with the studies herein demonstrating that ion pairing is more notable in less polar solvents, with coordination then present often in areas of greater positive charge density, and through hydrogen bonding of substrates.

3. Using DFT to Explore the Regioselectivity and Coordination in Gold(I) Catalysis

DFT has been used extensively to provide evidence and understanding to observed experimental results, with a view that by understanding reaction mechanism, then improvements or further development can then take place. This has been useful in gold chemistry, in the study of reaction regioselectivity, due to either carbon atom of the gold-coordinated unsaturated C–C bond being potential options for nucleophilic attack.

Amongst the simplest gold-catalysed reactions of alkenes and alkynes, are their hydration and hydroamination reactions, which typically progress via Markovnikov addition. However, methodologies are being published which accomplish the less-common anti-Markovnikov addition.

Timmerman *et al.* reported a gold(I)-catalysed hydroamination reaction of alkylidenecyclopropanes **13** (ACP) derivatives which resulted in the anti-Markovnikov addition of imidazolidone **14** (Figure 17).[25] Couce-Rios and co-authors used DFT to explore the origins of the observed regioselectivity.[26]

First, DFT was used to calculate the energies of the intermediates and transition states for the proposed mechanism, using the $\eta^2(\pi)$ gold(I)-coordinated benzyl-substituted

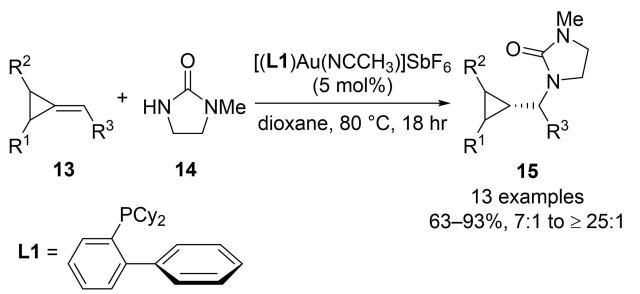

Figure 17. Gold(I)-catalysed hydroamination of ACP derivatives **13** with 1-methyl-imidazolidin-2-one **14** as reported by Timmerman *et al.*[25]

ACP derivative (**U**) as the reference compound. Energies (calculated at the M06/6-31G(d,p)&SDD(f) level of theory) of +21.7 and +21.0 kcal mol^{-1}, were calculated for the transition states of Markovnikov ($\mathbf{TS_{UW}}$) and anti-Markovnikov ($\mathbf{TS_{UV}}$) addition respectively (Figure 18).

When considering the relative energy difference between pathways, it is important to note that due to the logarithmic relationship between the calculated energy and both the equilibrium and rate constants, a small difference in energy can contribute to a significant difference in the predicted outcome.[27] In this instance, whilst the calculated energies of the transition states are similar, and a mixture of products might be predicted, the formation of **15** was seen predominantly via lower energy transition state $\mathbf{TS_{UV}}$, highlighting the need to consider both the experiments and calculations together.

The energies for the possible protiodemetallation pathways were also calculated, which suggested that the initial nucleophilic addition was the rate-determining step. The height of the energy barriers is consistent with the elevated temperature required for these reactions to occur.

Next, alkenes bearing various substituents were considered to compare the geometries of the $\eta^2(\pi)$-alkene gold(I) complex and the transition state energies for Markovnikov and anti-Markovnikov addition (Table 2). These data were then compared to the experimental results where available. It should be noted that all the calculations use CyJohnPhos (**L1**) as the ligand, however the experimental results of ethylene, styrene and isobutene were only available for TrixiePhos (**L2**).[28] Most of the experimental results match the predicted outcomes.[25,28] Alkenes **16a**, **16e**, **16g** and **16h** proceeded with Markovnikov addition, and alkene **16f** is the previously discussed benzyl-substituted ACP derivative, which occurred

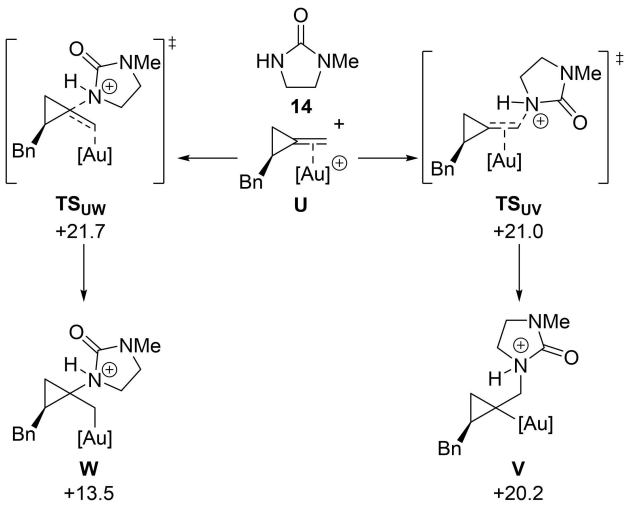

Figure 18. DFT-calculated transition state energies for Markovnikov and anti-Markovnikov addition into gold(I)-coordinated ACP **U**. Energies are Gibbs energies in kcal mol^{-1} at 298 K, calculated at the M06/6-31G(d,p)&SDD(f) level of theory with SMD solvent correction in 1,4-dioxane.

Table 2. Transition state energies for Markovnikov ($\Delta G_M^{\ddagger}$) and anti-Markovnikov ($\Delta G_{aM}^{\ddagger}$) addition of **14** catalysed by (L1)Au^+, and geometrical parameters for the initial $\eta^2(\pi)$-alkene gold(I) complexes. All data were computed at the M06/6-31G(d,p)&SDD(f) level of theory.

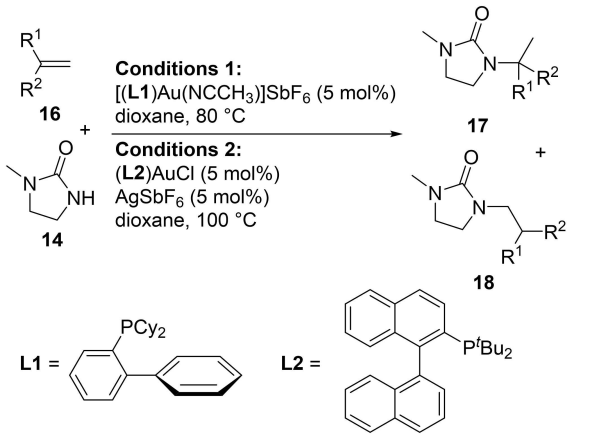

Substrate	$\Delta G_M^{\ddagger}$ / kcal mol^{-1}	$\Delta G_{aM}^{\ddagger}$ / kcal mol^{-1}	$\Delta\Delta G^{\ddagger}$ / kcal mol^{-1}	d_1-d_2[a] / Å	**17**:**18** Ratio
	+15.4		–	−0.002	100:0[c]
16a 	+23.2	+8.1	+15.1	0.007	–
16b 	+19.0	+10.6	+8.4	−0.002	–
16c 	+23.5	+16.1	+7.4	−0.105	–
16d 	+21.4	+19.4	+2.0	−0.154	100:0[c]
16e 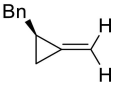	+21.7	+21.0	+0.7	−0.119	0:100[b]
16f 	+20.4	+27.4	−7.0	−0.257	100:0[c]
16g 	+20.0	+27.3	−7.3	−0.256	100:0[d]
16h					

[a] d_1 = Au–$C_{terminal}$ distance; d_2 = Au–$C_{internal}$ distance. [b] Conditions 1 were used. [c] Conditions 2 were used. [d] Conditions 1 were used at 100 °C.

with anti-Markovnikov addition. Styrene (**16e**) was the only example which the experimental outcome doesn't match the predicted outcome.

A trend was observed in which the energy difference between the Markovnikov and anti-Markovnikov addition could be related to the degree that the gold(I) catalyst has slipped across the alkene (Figure 19). Additional work by the group showed that strain from the disfavoured addition was significantly higher than the favoured addition, which further highlighted the importance of the initial geometry of the gold-coordinated alkene.

A similar substituent-directed effect was studied in the gold(I)-catalysed cyclisation of β-yne furans, reported by Dong *et al*, as a method to make cyclohexafuran and cycloheptafuran derivatives.[29] The cycloheptafuran skeleton is found in natural products,[30] but their synthesis is challenging using conventional methods.

With β-yne furans (*e.g.* **19**), nucleophilic attack can take place into the $\eta^2(\pi)$-alkyne gold(I)-coordinated complex (Figure 20), either through a 6-*exo* cyclisation (**19**→**22**) resulting in cyclohexafuran species **23**, or alternatively, attack can occur on the other carbon via a 7-*endo* cyclisation (**19**→**20**), giving cycloheptafuran derivatives **21**.

Typically, cyclohexafuran analogues are formed when reacting β-yne furans with transition metal catalysts (Figure 21a).[31] However, it was proposed by Dong *et al.* that tuning the electronic properties of the alkyne may allow for better control of the regioselectivity. Using internal alkyne **26**, it was possible to optimise for the formation of the desired cycloheptafuran product **27** using gold(I) catalysis (Figure 21b).

To explore the mechanism using DFT (at the B3LYP/SDD-6-31G(d) level of theory), transition states for the 7-*endo* ($\mathbf{TS_{XY}}$) and 6-*exo* ($\mathbf{TS_{XZ}}$) pathways were calculated (Figure 22), from $\eta^2(\pi)$-alkyne gold(I) complex **X**, for different

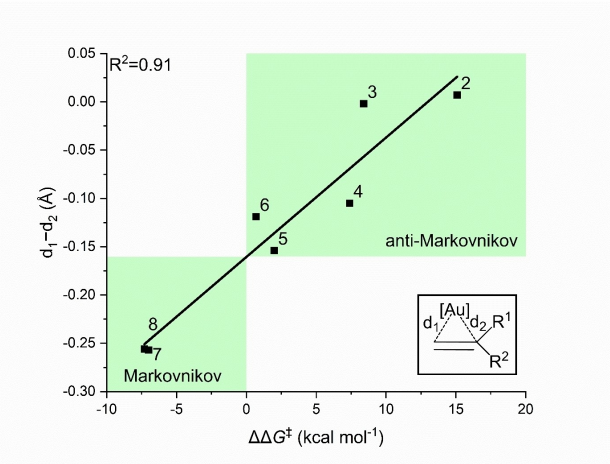

Figure 19. Plot of the difference in transition state energy between Markovnikov and anti-Markovnikov addition (ΔΔG‡) against the difference in distance of the gold centre from the terminal (d_1) and internal (d_2) carbons. Values refer to the entries in Table 2. Adapted with permission from ref [26]. Copyright 2019 American Chemical Society.

Israel Journal of Chemistry

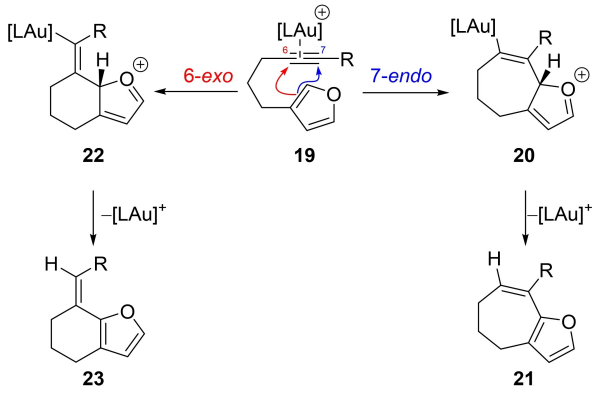

Figure 20. Proposed 6-*exo* and 7-*endo* cyclisations of β-yne furan derivative **19**.

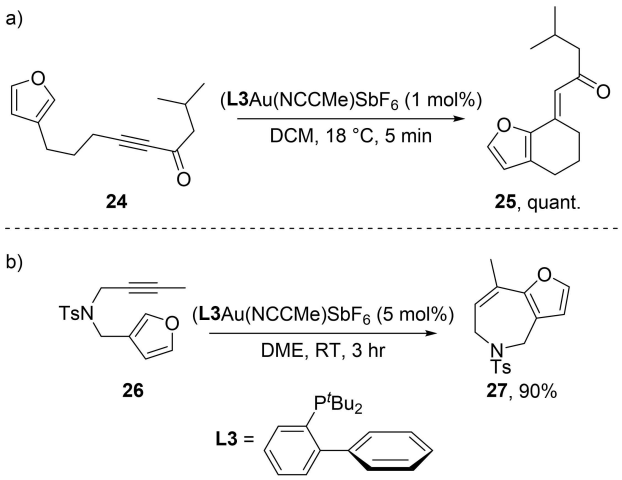

Figure 21. Synthesis of cyclohexafuran **20** as reported by Menon *et al.* in their total synthesis of furansesquiterpenes.[31d] b) Optimised conditions for the 7-endo-dig cyclisation of β-yne furan **21**.

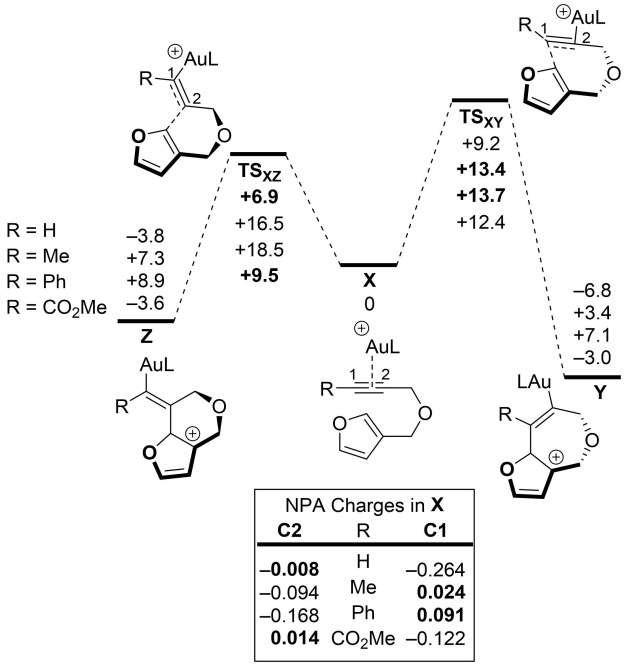

Figure 22. DFT-calculated energies for 6-exo and 7-endo cyclisation of β-yne furans. Energies are Gibbs energies at 298 K in kcal mol^{-1} at the B3LYP/SDD-6-31G(d) level of theory. Calculated NPA charges for the alkyne carbons of **X** are given. L=PMe_3. Reproduced with permission from ref [29]. Copyright 2013 Wiley-VCH.

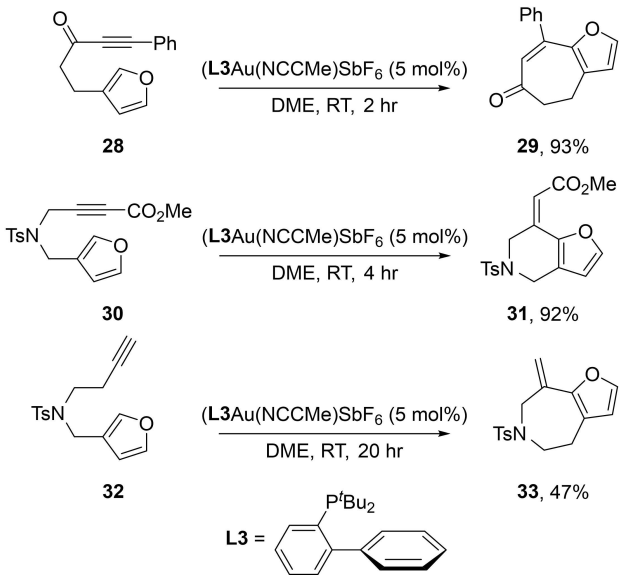

Figure 23. Additional reactions to explore the substrate scope following the DFT analysis.

substituents. This was successful at matching the experimental outcomes, with the terminal alkyne favouring the 6-*exo* transition state by 2.3 kcal mol^{-1}, and the methyl- and phenyl-substituted pathways favouring the 7-*endo* transition state by 3.1 and 4.8 kcal mol^{-1} respectively.

To determine the reasons between the difference in reaction outcome, natural population analysis (NPA) was used to compare the charges of the alkyne carbon atoms. This demonstrated that the different alkyne substituents affected the charge density of the alkyne, with nucleophilic attack then occurring onto the most 'positively' charged carbon of the alkyne. This then highlighted further ways the scope of the reaction could be expanded (Figure 23).

Firstly, introduction of a ketone on the tether to make an internal ynone moiety **28** still resulted in formation of the cycloheptafuran product **29**, which was proposed to be due to the synergistic effects of the substituents. Secondly, the calculations highlighted that substituting the alkyne with an ester functionality (**30**) would promote formation of the 6-*exo* products, which was observed experimentally (**31**). Finally, by extending the tether (**32**), 7-*exo* cyclisation could be achieved

Israel Journal of Chemistry

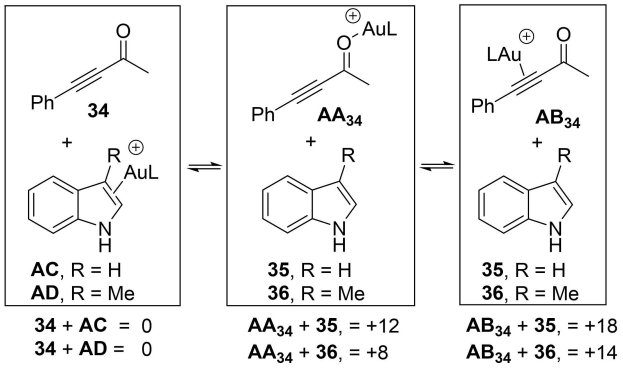

Figure 24. Energies are Gibbs energies at 298.15 K at the D3(BJ)–PBE0/def2-TZVPP//BP86/SV(P) level of theory with COSMO solvent correction in toluene. Energies are in kJ mol^{-1}. L=PPh_3.

with terminal alkynes (**33**). This highlights well the power of DFT to inform new directions for synthesis.

In our own groups, we have used DFT to explore the selectivity of gold(I) coordination in a study exploring the formation of 3-vinylindole species using alkynes with electron-withdrawing functionalities.[32] First, the relative energy difference between coordination to indoles (**35** and **36**) and ynone (**34**) species were compared (Figure 24). Coordination to both the ketone (**AA**) and alkyne (**AB**) of the ynone was considered. It was found that the indole gold(I)-coordinated species (**AC** and **AD**) was calculated to be the lowest energy-binding mode (at the D3(BJ)-PBE0/def2-TZVPP//BP86/SV(P) level of theory), followed by $\eta^1(O)$-binding (+12 and +8 kJ mol^{-1} for indole and skatole respectively), with $\eta^2(\pi)$-binding being the highest (+18 and +14 kJ mol^{-1} for indole **35** and skatole **36** respectively).

Due to the ability of the gold cation to coordinate to either the carbonyl or the alkyne, further calculations were performed to compare the affinity of the gold in a range of carbonyl-substituted alkynes (Figure 25a). Esters and amides were considered, both with and without a strong electron-donating substituent on the aryl group. $^{31}P\{^1H\}$ NMR spectra were then recorded with a 2 : 1 substrate to gold ratio (Figure 25b), and by comparing the chemical shifts observed with two reference species (DMF and an unsymmetrical *bis*-aryl alkyne, Figure 25c), conclusions were able to be made regarding the assignments of the resonances.

Coordination to the carbonyl was predicted to be favoured with amide **38**, and the resonance observed was consistent with the DMF reference (*e.g.* spectra (7) and (3)), at δ_P 29.7. Esters (**40** and **41**) were predicted to favour alkyne coordination and whilst ester **40** showed no evidence of coordination in NMR spectrum (5), a resonance at δ_P 35.8 was observed with the ester **41**, bearing an electron-donating 4-NMe_2-substitutent, consistent with coordination to the alkyne (*e.g.* spectra (4) and (2)). 4-NMe_2-substituted amide **39** was predicted to show coordination to both the carbonyl and alkyne, with both resonances indeed observed (spectrum (6)).

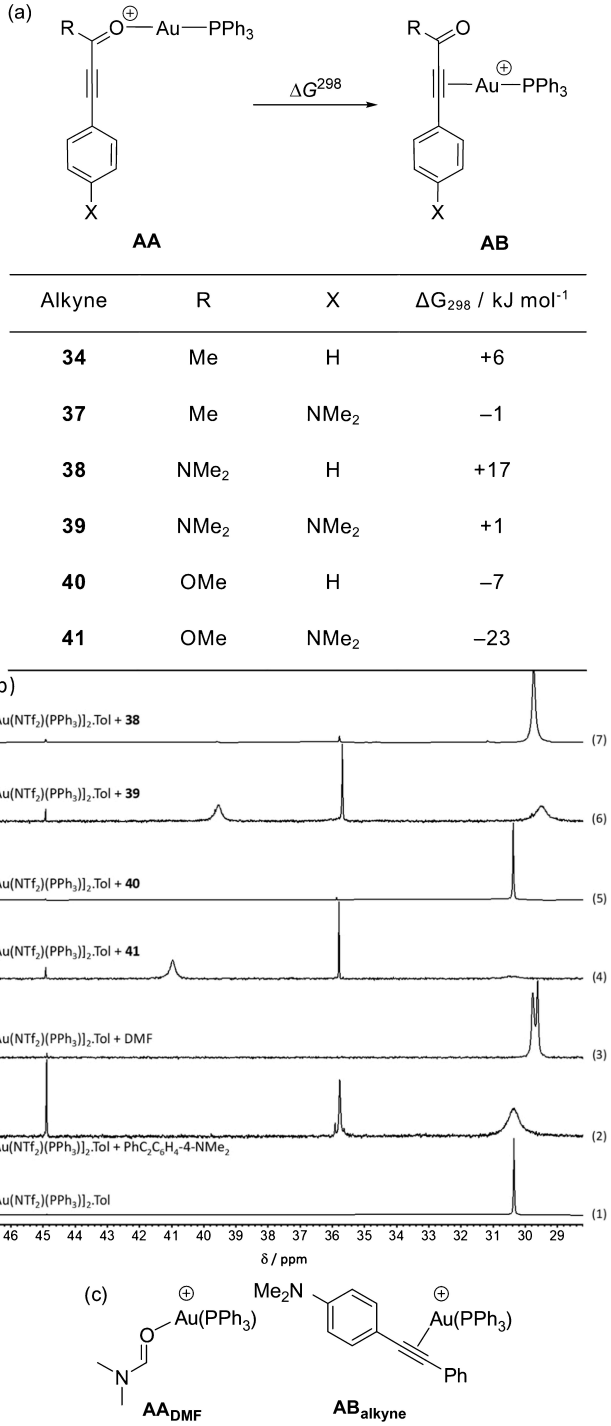

Alkyne	R	X	ΔG_{298} / kJ mol^{-1}
34	Me	H	+6
37	Me	NMe_2	–1
38	NMe_2	H	+17
39	NMe_2	NMe_2	+1
40	OMe	H	–7
41	OMe	NMe_2	–23

Figure 25. a) Isodesmic reaction used to compare $\eta^1(O)$-binding and $\eta^2(\pi)$-binding of substituted alkynes. Energies are Gibbs energies at 298.15 K at the in D3(BJ)–PBE0/def2-TZVPP//BP86/SV(P) level of theory with COSMO solvent correction in CH_2Cl_2. b) $^{31}P\{^1H\}$ NMR spectra in CD_2Cl_2 showing the interaction between $[(PPh_3)AuNTf_2]_2$.Tol and different substrates at a 2:1 substrate to gold ratio. c) Proposed $\eta^1(O)$-binding and $\eta^2(\pi)$-binding for DMF and $PhC_2C_6H_4$–4NMe_2 respectively.

Israel Journal of Chemistry

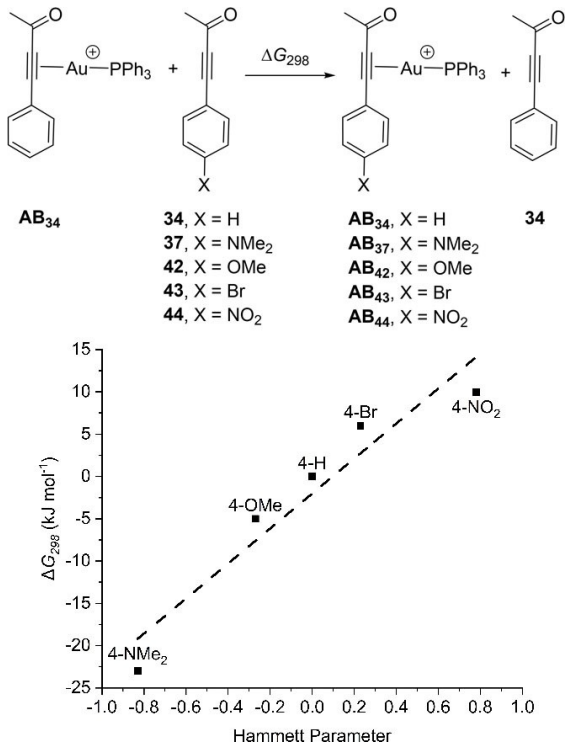

Figure 26. Isodesmic reaction used to calculate gold affinity for substituted alkynes. Energies are Gibbs energies at 298.15 K at the D3(BJ)–PBE0/def2-TZVPP//BP86/SV(P) level of theory with COSMO solvent correction in CH_2Cl_2 (top). Linear free energy relationship between the calculated change in energy and the Hammett parameter, σ_p. Dashed line shows the fit to a least mean squares linear regression ($R^2 = 0.92$) (bottom).

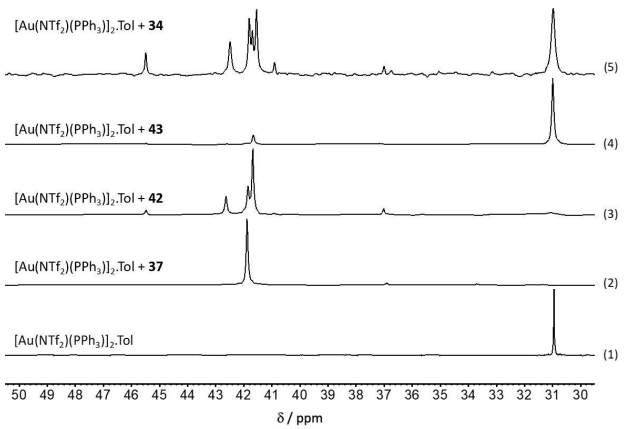

Figure 27. $^{31}P\{^1H\}$ NMR spectra in CD_2Cl_2 showing the interaction between $[(PPh_3)AuNTf_2]_2$.Tol and different ynones at a 10:1 substrate to gold ratio.

The effects of substitution on the aryl group were also considered, and the isodesmic reaction between $\eta^2(\pi)$-coordinated alkyne **AB_{34}** and uncoordinated alkynes with both electron-donating and withdrawing groups were considered. A

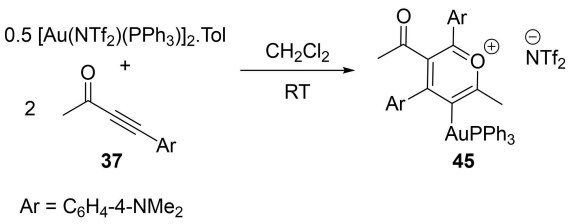

Figure 28. Formation of pyrylium salt **45** from the dimerisation of ynone **37**.

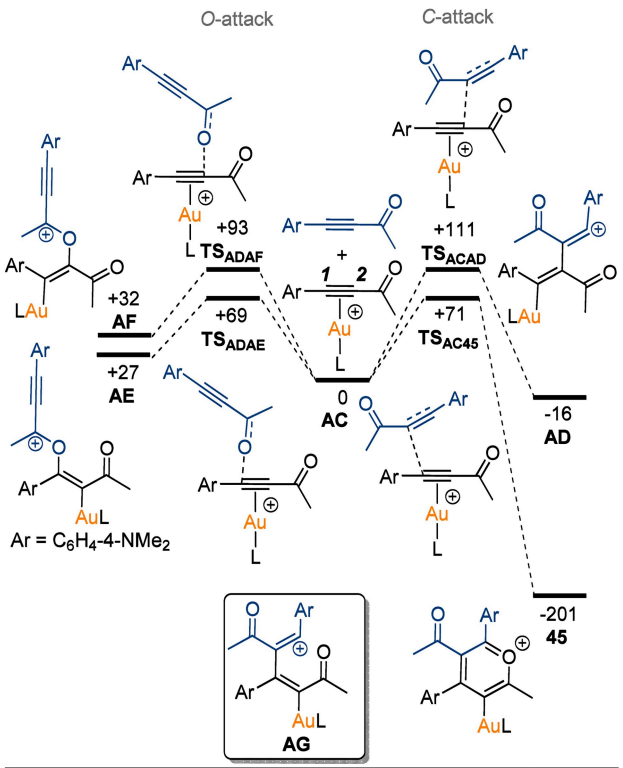

Ar	L	TS_{AC45}	TS_{ADAE}	AE	45
C_6H_4-4-NMe_2	PPh_3	+71	+69	+27	–201
C_6H_5	PPh_3	+75	+63	+23	–224
C_6H_4-4-OMe	PPh_3	+69	+61	+20	–220
C_6H_4-4-NMe_2	PMe_3	+61	+70	+33	–197
C_6H_4-4-NMe_2	IPr	+77	+77	+33	–198
C_6H_4-4-NMe_2	John Phos	+70	+75	+37	–199

Figure 29. DFT-calculated pathways of gold-mediated ynone dimerisation. Energies are Gibbs energies at 298.15 K in kJ mol^{-1} at the D3(BJ)–PBE0/def2-TZVPP//BP86/SV(P) level of theory with solvent correction in CH_2Cl_2.

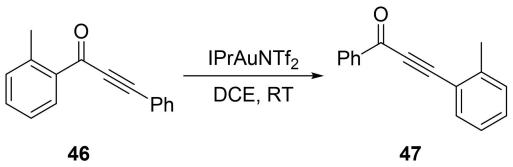

Figure 30. Gold-catalysed transposition reaction of ynone **46**.

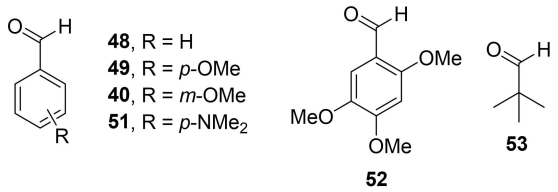

Figure 32. Aldehydes used in the further studies.

Hammett plot of the energy difference demonstrated a strong substituent effect on the nature of the equilibrium (Figure 26).

$^{31}P\{^{1}H\}$ NMR spectra were recorded with a large excess of substrate (10 : 1 substrate to gold ratio, Figure 27) which supported the DFT-predicted enhanced gold affinity for electron-rich alkynes. The NMR spectra with 4-Br substituted ynone **43** and unsubstituted ynone **34** showed a large amount of remaining uncoordinated catalyst (*e.g.* spectra (4), (5) and (1)). Ynone **34** (spectrum (5)) did show a series of new resonances in the region between δ_P 40 and 45. The 4-OMe substituted ynone **42** showed full coordination of the gold catalyst but as before a complex set of resonances were again observed (spectrum (3)).

Considering the NMR spectrum of 4-NMe_2-substituted ynone **37** (spectrum (2)), only a single sharp resonance at δ_P 41.9 was present, inconsistent with either carbonyl or alkyne coordination. Through further NMR and mass spectroscopy studies, this was assigned as a gold-pyrylium complex (**45**), arising from the dimerisation of the ynone (Figure 28).

DFT was used to examine the dimerisation mechanism in detail (Figure 29). It was proposed that dimerisation occurred via *C*-attack of the alkyne of one ynone into the $\eta^2(\pi)$-coordinated alkyne of another ynone ($\mathbf{TS_{AC45}}$). The calculated transition state energy for this was $+71\ kJ\,mol^{-1}$ from reference state **AC**. This would then be followed by an intramolecular *O*-cyclisation from intermediate **AG** to afford the gold-pyrylium complex **45**, with an overall energy of $-201\ kJ\,mol^{-1}$ for the process. A structure for intermediate carbocation **AG** couldn't be located, suggesting that either there is a bifurcated pathway from $\mathbf{TS_{AC45}}$ to the pyrylium complex, or that **AG** sits in a shallow minimum.

To further explore the dimerisation process, the transition state for *C*-attack onto the C2 carbon of the alkyne was found ($\mathbf{TS_{ACAD}}$) which was calculated to be much higher in energy ($+111\ kJ\,mol^{-1}$). Additionally, two transition states were located for oxo-nucleophilic attack of the carbonyl at $+69$ ($\mathbf{TS_{ADAE}}$) and $+93\ kJ\,mol^{-1}$ ($\mathbf{TS_{ADAF}}$). It was proposed that the

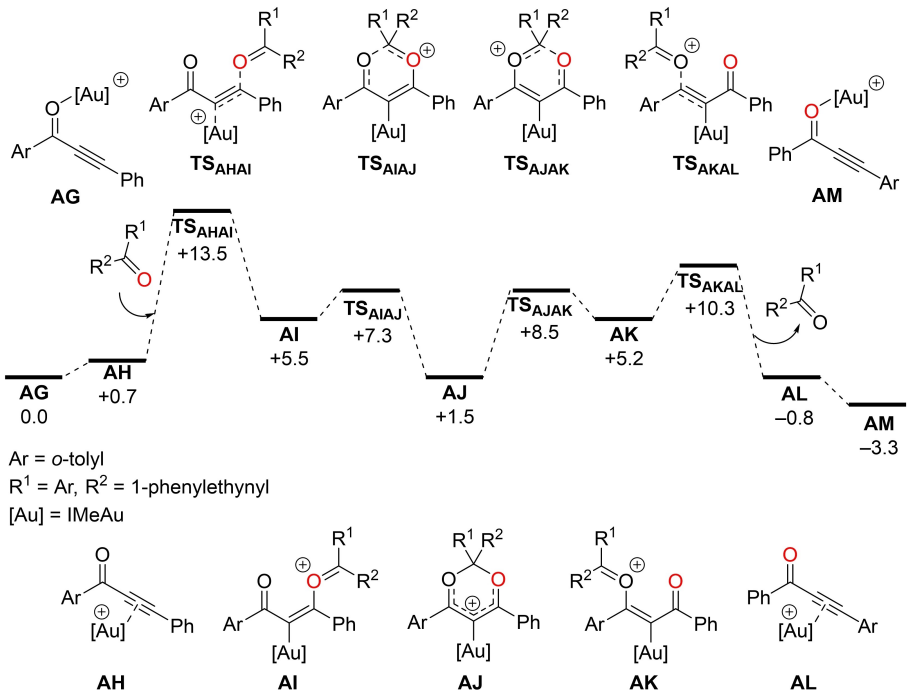

Figure 31. DFT-calculated energies for the gold-catalysed 1,3 transposition of ynone **46**. Energies are Gibbs energies at the TPSS-D3/def2-TZVP//TPSS-D3/def2-SVP level of theory in kcal mol^{-1} with COSMO solvent correction in CH_2Cl_2. Reproduced with permission from ref [33]. Copyright 2019 American Chemical Society.

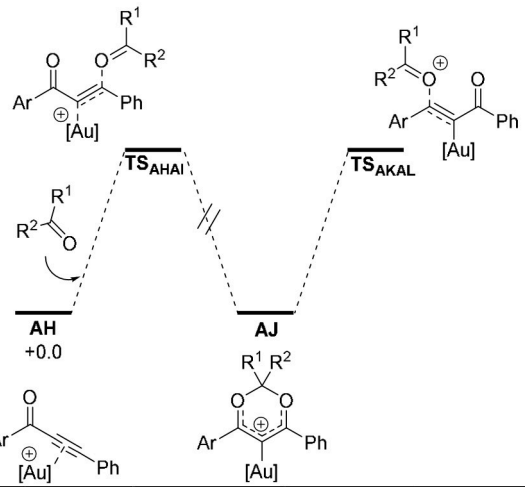

Entry	Additive	ΔG (TS$_{AHAI}$–AH) / kcal mol^{-1}	ΔG (AJ–AH) / kcal mol^{-1}	ΔG (TS$_{AKAL}$–AJ) / kcal mol^{-1}
1	**46**	+13.5	+1.5	+8.9
2	**47**	+14.4	+2.1	+8.5
3	**48**	+14.9	−4.7	+18.7
4	**49**	+12.8	−2.3	+13.4
5	**50**	+14.1	−4.4	+17.1
6	**51**	+11.3	−1.3	+9.0
7	**52**	+10.5	−2.4	+11.3
8	**53**	+15.3	−9.9	+22.0

Figure 33. DFT-calculated energies for the key transition states and intermediates of the gold-catalysed transposition reaction of ynones with different additives. Energies are Gibbs energies at the TPSS-D3/def2-TZVP//TPSS-D3/def2-SVP level of theory with COSMO solvent correction in CH_2Cl_2. Reproduced with permission from ref [33]. Copyright 2019 American Chemical Society.

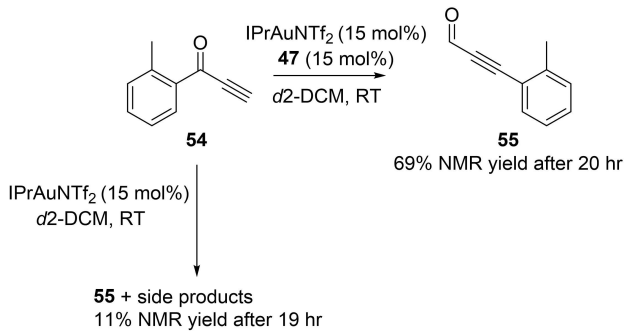

Figure 34. Transposition reaction using challenging substrate **54**.

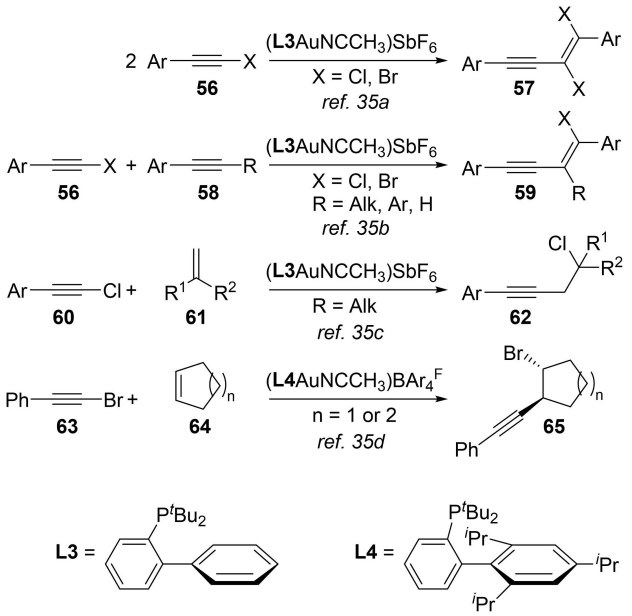

Figure 35. Gold(I)-catalysed 1,2-haloalkynylation reactions of haloalkynes, alkynes and alkenes.

strong thermodynamic driving force for the formation of the pyrylium complex causes its irreversible formation.

Additional calculations were done to compare the energies of the transition states and intermediates for the lowest energy additions of both *C*- and *O*-attack, for both the unsubstituted (**34**) and 4-OMe-substituted ynones (**42**). In contrast to the 4-NMe_2-substituted ynone, *O*-attack was calculated to be the lowest energy transition state for both substrates, and it was proposed that the lack of selectivity observed in the NMR spectra (Figure 27) discussed originated from side-reactions of **AE**. The effect of the ligand was also explored; however, this was predicted to have little to no effect on the experimental outcomes.

In 2018, Aikonen and co-workers studied the gold-catalysed 1,3-*O*-transpoisition of ynones (Figure 30).[33] Initial kinetic studies highlighted that there was an order in **46** of 1.5 and a small order of 0.15 for **47**, thus two ynone molecules are required in the rate-determining step.

An intermolecular mechanism was therefore proposed, with the energies calculated using DFT (at the TPSS-D3/def2-TZVP//TPSS-D3/def2-SVP level of theory, Figure 31), in which *O*-attack of the carbonyl of one ynone, into the $\eta^2(\pi)$-coordinated alkyne of another ynone occurs with a calculated energy of $+13.5\ kcal\,mol^{-1}$ (**TS$_{AHAI}$**), followed by a low energy transition state of $+7.3\ kcal\,mol^{-1}$ for intramolecular cyclisation (**TS$_{AIAJ}$**) to form cyclic acetal complex **AJ**. This process then happens in reverse, with the overall reaction yielding an unchanged ynone, and one in which the position of the carbonyl has changed.

It was noted that the carbonyl of the uncoordinated ynone acts as a nucleophile, so studies were performed to see if using an electron-rich aldehyde can increase the rate of reaction. A

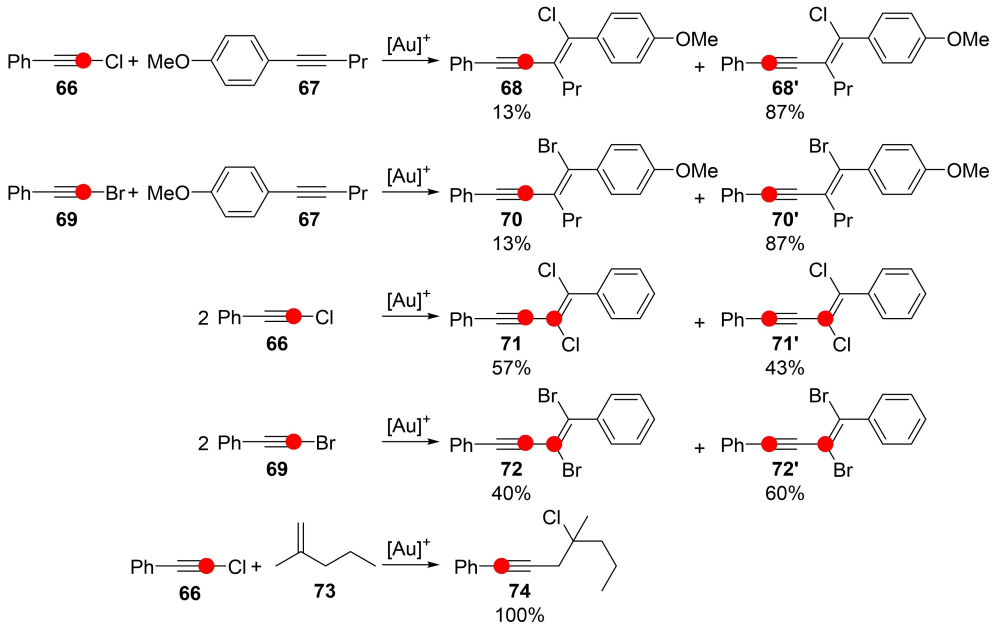

Figure 36. ^{13}C-labelling experiments of 1,2-haloalkynylation reactions. The red circled atoms denote ^{13}C-labelled atoms. $[Au]^+$ =(JohnPhosAuNCMe)$^+$.

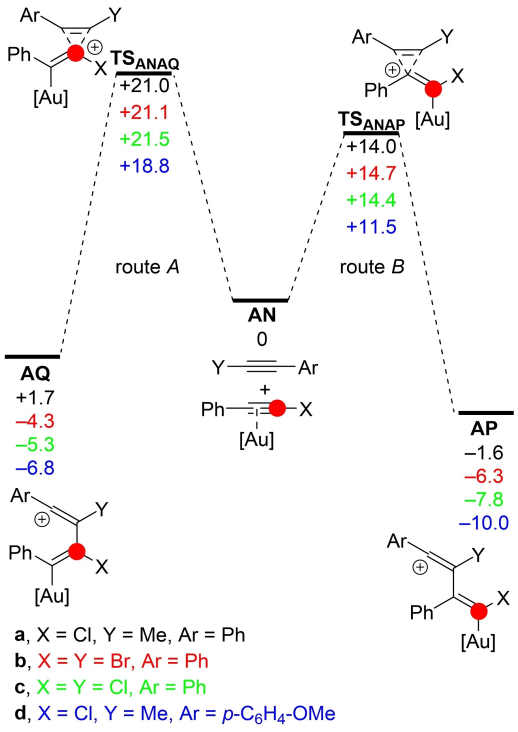

Figure 37. DFT-calculated energies for the initial nucleophilic attack in gold(I)-coordinated alkyne. Energies are Gibbs energies in kcal mol^{-1} at the B3LYP-D3BJ//6-311++G(d,p),def2TZVP//B3LYP-D3BJ/6-31G(d),def2-TZVP level of theory with SMD solvent correction in DCE. [Au]=JohnPhosAu$^+$.

range of substituted aldehydes (Figure 32) were tested experimentally, and it was shown that the aldehyde did have a marked effect on the reaction rate, with benzaldehydes bearing electron-donating functionalities in conjugation with the aldehyde showing the greatest increase in reaction rate.

The DFT-calculated energies of the highest transition state barriers ($\mathbf{TS_{AHAI}}$ and $\mathbf{TS_{AKAL}}$) were compared to the $\eta^2(\pi)$-coordinated alkyne **AH** and the cyclic acetal complex **AJ**, for the different additives (Figure 33). This showed a difference in the transition state energies that correlated with the experimental rate differences, with aldehyde **52** showing the largest energy decrease for transition state $\mathbf{TS_{AHAI}}$.

Furthermore, the energy of the transition state for loss of aldehyde ($\mathbf{TS_{AKAL}}$), was calculated to be higher when pivaldehyde **53** was used (+22 kcal mol^{-1}) suggesting a greater kinetic stability for the cyclic acetal intermediate. When the transposition reaction was done with **53** at 15 °C, the characterisation of the cyclic acetal intermediate was possible by recording ^{1}H and 2D NMR spectra at 15 °C and 0 °C respectively.

Additionally, using this improved methodology allowed for a challenging transposition reaction with terminal alkyne **54** (Figure 34). A marked improvement in the NMR yield of **55** was observed, from 11% to 69%, with fewer side products.

Recent work published by Kreuzahler and Haberhauer,[34] explored the mechanism of the gold(I)-catalysed 1,2-haloalkynylation reactions of haloalkynes,[35a] alkynes[35b] and alkenes[35c,d] (Figure 35) using DFT and ^{13}C-labelling, to compare previously proposed mechanisms.

^{13}C-labelling experiments (Figure 36) determined that in the 1,2-haloalkynylation of internal alkyne **67**, the ^{13}C-labelled

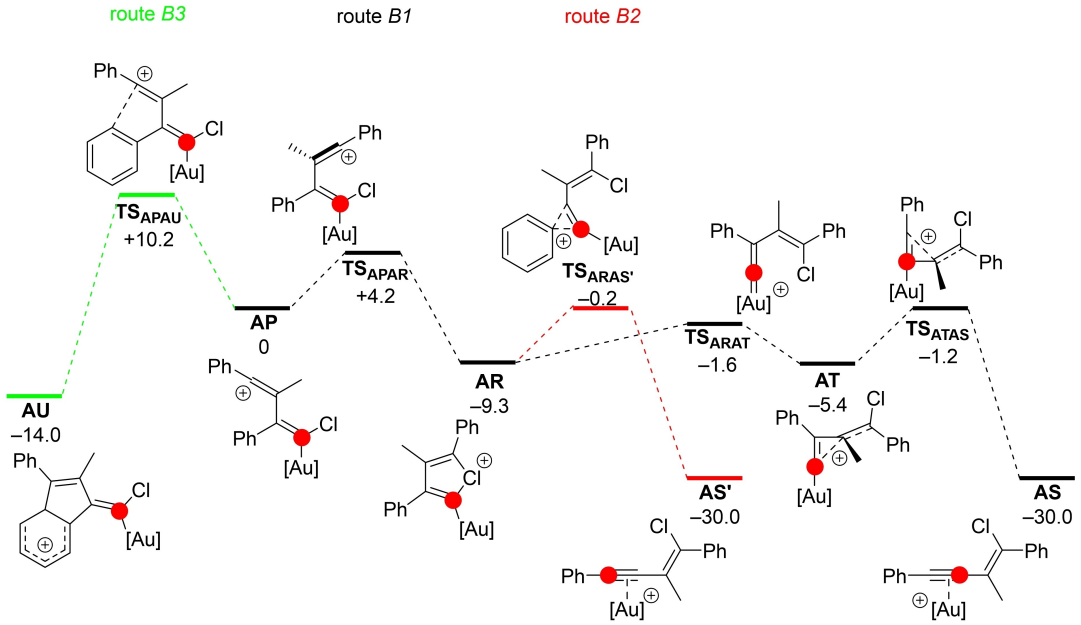

Figure 38. DFT-calculated energies of possible reaction routes from **AP**. Energies are Gibbs energies in kcal mol^{-1} at the B3LYP-D3BJ//6-311++G(d,p),def2TZVP//B3LYP-D3BJ/6-31G(d),def2-TZVP level of theory with SMD solvent correction in DCE. [Au] = JohnPhosAu^{+}.

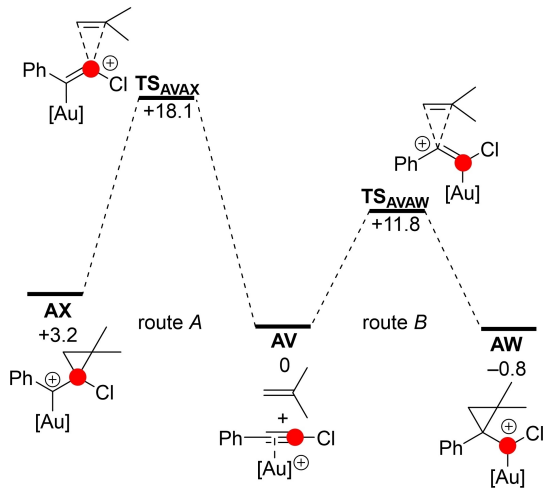

Figure 39. DFT-calculated energies for the initial nucleophilic attack in gold(I)-coordinated alkyne with isobutene. Energies are Gibbs energies in kcal mol^{-1} at the B3LYP-D3BJ//6-311++G-(d,p),def2TZVP//B3LYP-D3BJ/6-31G(d),def2-TZVP level of theory with SMD solvent correction in DCE. [Au] = JohnPhosAu^{+}.

atom was heavily biased to be closest to the aryl group in both alkyne products **68** (with chlorophenylacetylene **66**) and **70** (with bromophenylacetylene **69**). Further work which studied the dimerisation reactions of **66** and **69** showed a much less biased distribution of ^{13}C-labelled atoms, and the 1,2-haloalkylation reaction with alkene **73** showed a single product (**74**). It was proposed that the selectivity was determined during the initial step and the observed distribution was related to the relative transition state energies.

Initially, the energies of the transition states from both sites of possible nucleophilic attack of an alkyne into the $\eta^2(\pi)$-alkyne gold(I) complex were calculated (Figure 37). A range of alkynes were considered and, in each case, route B was significantly lower in energy than route A (7.0–7.4 kcal mol^{-1}), corresponding to preferential attack adjacent to the aryl group of the gold(I)-coordinated alkyne (**TS$_{ANAP}$**). Due to the large difference in energies between the two transition states, only a single product isomer of **68**, **70**, **71** and **72** would be expected, if the initial nucleophilic step was key as initially proposed, therefore, the reactivity of carbocation **AP** and **AQ** was considered. Herein only carbocation **AP**, from the lowest energy pathway will be discussed.

Considering vinyl cation **AP** (Figure 38), a transition state for the formation of bicyclic indene complex **AU** was found, however this pathway was predicted to be 8.3 kcal mol^{-1} in energy higher than the formation of chloronium complex **AR**. This complex can then form enyne **AS′** via direct phenyl migration **TS$_{ARAS'}$**, or alternatively, via unusual cyclopropenylmethyl cation **AT** (discussed further in the paper), which facilitates an alkyl-migration via transition state **TS$_{ATAS}$** to also yield enyne **AS**, with the ^{13}C-labelled carbon in a different position. These two pathways are predicted to differ only by an energy of 1.0 kcal mol^{-1} and therefore both pathways could be expected to be followed. It should be highlighted here that no direct experimental outcome can be compared as 1-phenyl-1-propyne was used as a model substrate.

A similar series of calculations were performed for the addition of isobutene into chlorophenylacetylene **66**. Again, both possible transition states were considered for the initial

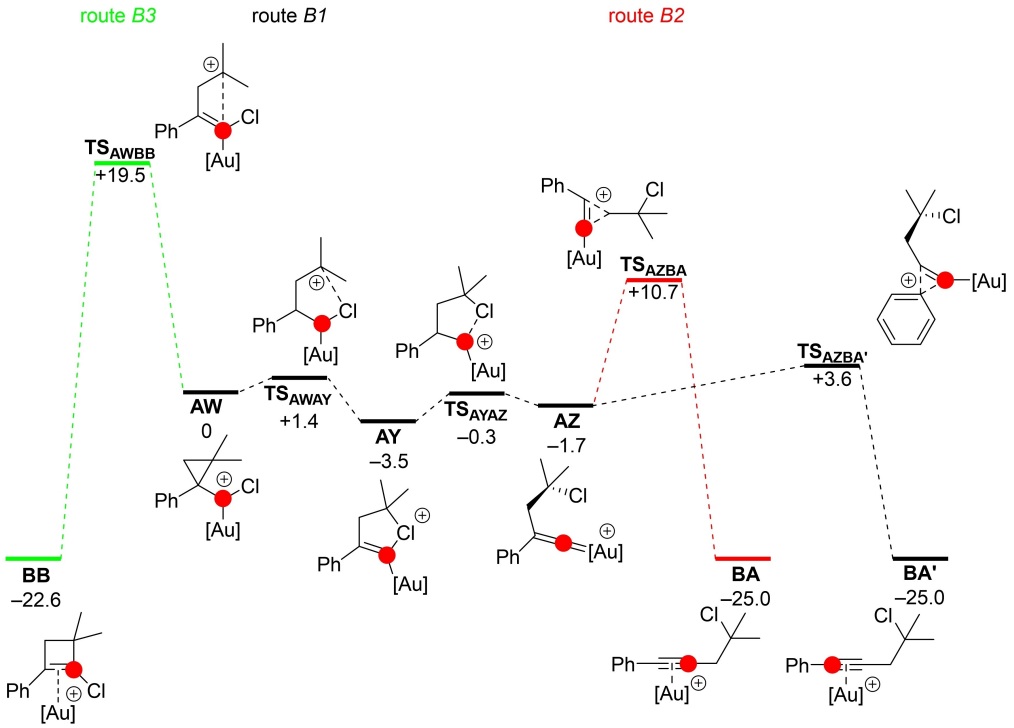

Figure 40. DFT-calculated energies of possible reaction routes from **AW**. Energies are Gibbs energies in kcal mol^{-1} at the B3LYP-D3BJ//6-311++G(d,p),def2TZVP//B3LYP-D3BJ/6-31G(d),def2-TZVP level of theory with SMD solvent correction in DCE. [Au] = JohnPhosAu^{+}.

nucleophilic attack in to the $\eta^2(\pi)$-alkyne gold(I)-coordinated complex (Figure 39), with addition into the alkyne directly next to the aryl group predicted to be favoured by 6.3 kcal mol^{-1} via transition state **TS$_{AVAW}$**. The authors considered the reactivity of carbocation **AW** and **AX**, however, only carbocation **AW**, from the lowest energy pathway will be discussed here.

The fate of carbocation **AW** was considered (Figure 40). A transition state for a cyclisation was found (**TS$_{AWBB}$**) but this was calculated to be 18.1 kcal mol^{-1} higher in energy than the transition state for chlorine migration (**TS$_{AWAY}$**). The resulting chloronium cation (**AY**) can then further migrate to gold(I)-vinylidene complex **AZ** via low-lying transition state **TS$_{AYAZ}$** (−0.3 kcal mol^{-1} from carbocation **AY**). From vinylidene complex **AZ**, either an aryl (**TS$_{AZBA'}$**) or alkyl (**TS$_{AZBA}$**) migration can take place, but the transition state energy for aryl migration is lower by 7.1 kcal mol^{-1}, so it was proposed that this was the only accessible pathway. This results in alkyne product **BA'** which matches the experimentally observed position of the ^{13}C-labelled atom.

With the key transition states that control the position of ^{13}C-labelled atom of the haloalkynylation reaction now known, substituent effects were then considered (Figure 41). The transition states **TS$_{ARAS}$·d** and **TS$_{ATAS}$d** were found to only have a 0.6 kcal mol^{-1} difference in energy when the *p*-methoxy-substituted alkyne (**d** in Figure 41) was investigated. This alkyne was selected as an analogue of **67** to directly compare the experimental outcome (Figure 36) more accurately. The gold(I)-catalysed dimerisation of chlorophenylacetylene **66** was considered, and a 1.9 kcal mol^{-1} energy difference between routes B2 and B1, in favour of route B1, was found. This matches the experimentally observed outcome for the ^{13}C-labelled position, albeit slightly, with 57% of β-aryl labelled product **72** formed. When the dimerisation of bromophenylacetylene **69** was considered, route B1 was again predicted to be lower in energy by 2.4 kcal mol^{-1}. Whilst it might be expected that experimentally the ratio of β-aryl labelled product **72** should increase, instead a 60% yield of α-aryl labelled product **72′** was achieved, further highlighting that care must be taken when working with calculated relative energy differences which are small, with experimental benchmarking required.

A more significant selectivity effect was observed when comparing the effect of different ligands on the haloalkynylation reaction (Figure 42). Using trimethylphosphine instead of JohnPhos as the gold ligand in the calculations showed a significant change in the predicted selectivity. For the reaction of chlorophenylacetylene **66** and 1-methoxy-4-(prop-1-yn-1-yl)benzene (**d** and **g**), the transition state energy for route B1 using trimethylphosphine (**TS$_{ARAT}$g**) was increased to be above that of route B2 (**TS$_{ARAS}$·g**) by 1.4 kcal mol^{-1}. Experimentally (Figure 43), an increased yield of the α-aryl labelled product **68′** was observed, more closely matching the DFT-predicted outcome.

Furthermore, a similar effect was observed with the dimerisation of chlorophenylacetylene **66**. Instead of an energy

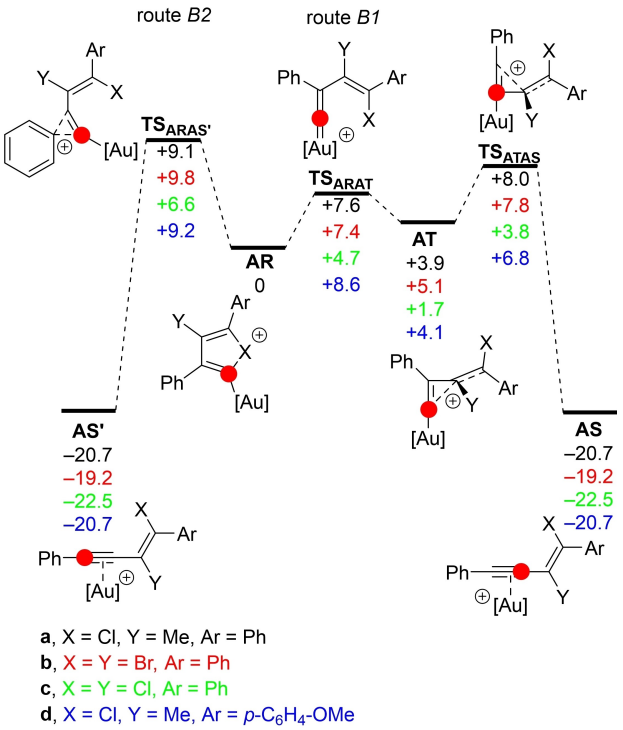

Figure 41. DFT-calculated energies of possible reaction routes from **AR**, with different reactants. Energies are Gibbs energies in kcal mol^{-1} at the B3LYP-D3BJ//6-311++G(d,p),def2TZVP//B3LYP-D3BJ/6-31G(d),def2-TZVP level of theory with SMD solvent correction in DCE. [Au]=JohnPhos^{+}.

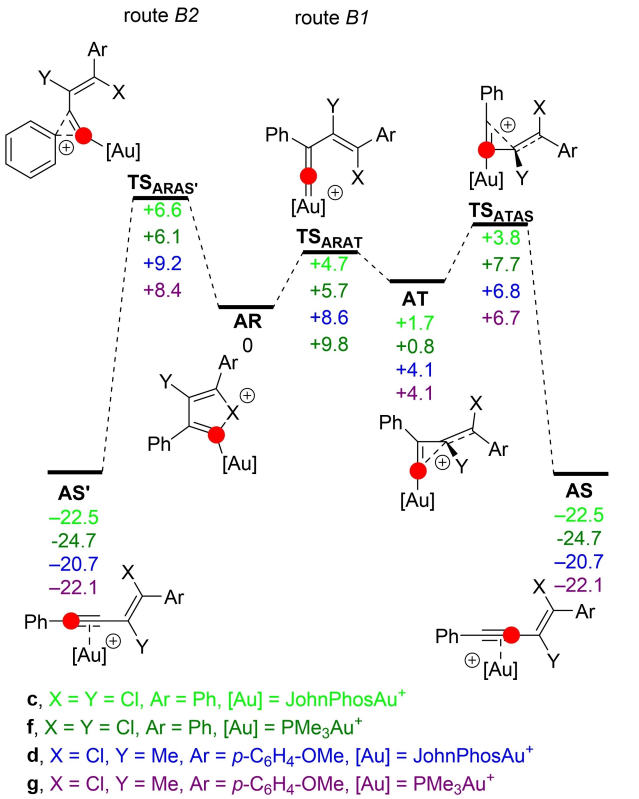

Figure 42. DFT-calculated energies of possible reaction routes from **AR**, with different ligands. Energies are Gibbs energies in kcal mol^{-1} at the B3LYP-D3BJ//6-311++G(d,p),def2TZVP//B3LYP-D3BJ/6-31G(d),def2-TZVP level of theory with SMD solvent correction in DCE.

difference of 1.9 kcal mol^{-1} in favour of route B1 (**TS$_{ARAT}$c**) with JohnPhos, the selectivity was reversed and route B2 (**TS$_{ARAS'}$f**) was favoured by an energy difference of 1.6 kcal mol^{-1}. Experimentally (Figure 43), rather than a 57:43 ratio of products, a 7:93 ratio was observed, with a higher amount of ^{13}C-labelling being next to the alkene (**71′**), matching the DFT-predicted outcome.

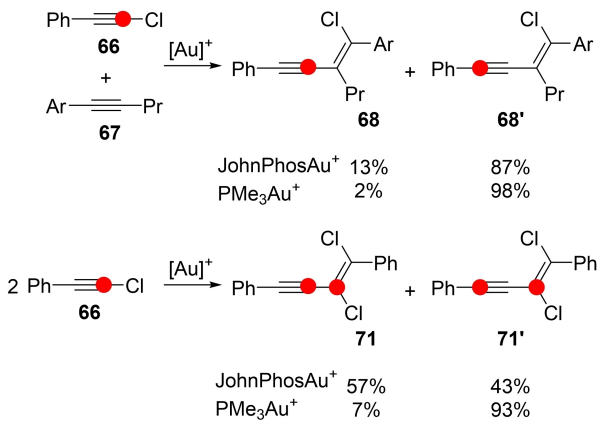

Figure 43. Reactions comparing the ^{13}C-labelling of 1,2-haloalkynylation reactions using JohnPhosAu^{+} and PMe$_3$Au^{+}. Ar=C$_6$H$_4$-4-OMe.

4. Summary

Computational chemistry can be an extremely useful tool to better understand reactions when used correctly, with the examples detailed herein demonstrating some such uses in gold(I) catalysis. However, as well as considering the level of theory used, care must also be taken that what is being modelled is an accurate description of the experimental conditions. This includes factors such as using a reasonable conformation of the molecules, factoring solvation into the calculations and whether to include the anion in the reaction.

The question of whether to include the anion from the gold(I) precatalyst in the calculation appears to be best answered on a case-by-case basis. In non-polar solvents, ion separation is not as pronounced, so a consideration of anion effects is particularly important – typically locating this in areas where a positive charge is localised or in positions that hydrogen-bonding can occur. If the reaction modelled directly involves groups where hydrogen-bonding is possible, alcohols or amines for example, then the anion could potentially have a pronounced effect on the observed energies calculated. In

these cases, then it is proposed that the anion should be modelled explicitly, especially if the DFT model does not agree with experiment. In the case of close-contact ion-pairs, then additional evidence may need to be gathered to determine the topology of the ensemble.

Using DFT to explore the selectivity of gold(I)-catalysed reactions is a natural fit due to the often-unsymmetrical nature of the unsaturated C–C bonds which gold chemistry is famed for activating. The regioselectivity can often be accurately predicted by DFT, which can then lead to the development of new substrates or different ligands to see if the selectivity can be improved or altered. Therefore, care must be taken to ensure that over-analysis of small-energy differences does not contradict the experimental outcomes.

Benchmarking the DFT results with comparison to the experiment is key to ensure that the model used is an accurate description. Utilising methods such as NMR spectroscopy and *in situ* IR to monitor reactions in progress could provide the evidence which helps verify the model used. Additionally, exploring the kinetic profile of the reaction and comparing with the calculated transition-state energies is also important.

Acknowledgements

We are grateful to the University of York for PhD studentship to funding to R. G. E. and the EPSRC (EP/H011455/1 and EP/K031589/1) for funding computational equipment used in this study.

References

[1] For the editorial of a recent *Chemical Reviews* special issue looking at the 'hot topics' in gold chemistry, see: A. S. K. Hashmi, *Chem. Rev.* **2021**, *121*, 8309–8310.

[2] a) L. Ciano, N. Fey, C. J. V. Halliday, J. M. Lynam, L. M. Milner, N. Mistry, N. E. Pridmore, N. S. Townsend, A. C. Whitwood, *Chem. Commun.* **2015**, *51*, 9702–9705; b) N. Hidalgo, J. J. Moreno, M. Pérez-Jiménez, C. Maya, J. López-Serrano, J. Campos, *Organometallics* **2020**, *39*, 2534–2544.

[3] a) R. L. LaLonde, W. E. Brenzovich Jr., D. Benitez, E. Tkatchouk, K. Kelley, W. A. Goddard III, F. D. Toste, *Chem. Sci.* **2010**, *1*, 226–233; b) Y. Zhu, W. Zhou, E. M. Petryna, B. R. Rogers, C. S. Day, A. C. Jones, *ACS Catal.* **2016**, *6*, 7357–7362.

[4] a) K. L. Toups, G. T. Liu, R. A. Widenhoefer, *J. Organomet. Chem.* **2009**, *694*, 571–575; b) L. Lempke, T. Fischer, J. Bell, W. Kraus, K. Rurack, N. Krause, *Org. Biomol. Chem.* **2015**, *13*, 3787–3791.

[5] a) R. Dorel, A. M. Echanvarren, *Chem. Rev.* **2015**, *115*, 9028–9072; b) A. Fürstner, P. W. Davies, *Angew. Chem. Int. Ed.* **2007**, *46*, 3410–3449; *Angew. Chem.* **2007**, *119*, 3478–3519; c) Y. Yamamoto, *J. Org. Chem.* **2007**, *72*, 7817–7831.

[6] a) D. J. Gorin, B. D. Sherry, F. D. Toste, *Chem. Rev.* **2008**, *108*,3351–3378; b) Z. Lu, T. Li, S. R. Mudshinge, B. Xu, G. B. Hammond, *Chem. Rev.* **2021**, *121*, 8452–8477.

[7] For general reviews of DFT use within homogenous transition metal catalysis, see: a) W. M. C. Sameera, F. Maseras, *WIREs Comput. Mol. Sci.* **2012**, *2*, 375–385; b) C. J. Cramer, D. G. Truhlar, *Phys. Chem. Chem. Phys.* **2009**, *11*, 10757–10816; c) P. Sit, L. Zhang, *Heterogeneous Catalysts: Advanced Design, Characterization and Applications, II*, Vol. 1 (Eds: W. Y. Teoh, A. Urakawa, Y. H. Ng, P. Sit), Wiley-VCH, Weinheim **2021**, pp. 405–418.

[8] a) O. N. Faza, R. A. Rodríguez, C. S. López, *Theor. Chem. Acc.* **2011**, *128*, 647–661; b) P. Nava, D. Hagebaum-Reignier, S. Humbel, *ChemPhysChem* **2012**, *13*, 2090–2096; c) R. Kang, W. Lai, J. Yao, S. Shaik, H. Chen, *J. Chem. Theory Comput.* **2012**, *8*, 3119–3127; d) G. Ciancaleoni, S. Rampino, D. Zuccaccia, F. Tarantelli, P. Belanzoni, L. Belpassi, *J. Chem. Theory Comput.* **2014**, *10*, 1021–1034; e) K. P. Kepp, *J. Phys. Chem. A* **2017**, *121*, 2022–2034.

[9] a) M. Bandini, A. Bottoni, M. Chiarucci, G. Cera, G. P. Miscione, *J. Am. Chem. Soc.* **2012**, *134*, 20690–20700; b) Y. Li, X. Zhao, *ChemCatChem* **2020**, *12*, 6265–6271; c) Y. Yang, J. Li, R. Zhu, C. Liu, D. Zhang, *ACS Catal.* **2018**, *8*, 9252–9261; d) A. A. Hussein, H. S. Ali, *J. Org. Chem.* **2020**, *85*, 12682–12691; e) L. Zhou, Y. Zhang, R. Fang, L. Yang, *ACS Omega* **2018**, *3*, 9339–9347; f) R. Fang, L. Zhou, P.-C. Tu, A. M. Kirillov, L. Yang, *Organometallics* **2018**, *37*, 1927–1936; g) B. Alcaide, P. Almendros, I. Fernández, R. Martín-Montero, F. Martínez-Peña, M. Pilar Ruiz, M. Rosario Torres, *ACS Catal.* **2015**, *5*, 4842–4845; h) Y. Li, J. Zhang, X. Zhao, Y. Wang, *J. Mol. Catal.* **2022**, *519*, 112154.

[10] a) B. Ranieri, I. Escofet, A. M. Echavarren, *Org. Biomol. Chem.* **2015**, *13*, 7103–7118; b) Z. Lu, G. B. Hammond, B. Xu, *Acc. Chem. Res.* **2019**, *52*, 1275–1288; c) Z. Lu, J. Han, O. E. Okoromoba, N. Shimizu, H. Amii, C. F. Tormena, G. B. Hammond, B. Xu, *Org. Lett.* **2017**, *19*, 5848–5851.

[11] a) J. H. Teles, S. Brode, M. Chabanas, *Angew. Chem. Int. Ed.* **1998**, *37*, 1415–1418; *Angew. Chem.* **1998**, *110*, 1475–1478; b) E. Mizushima, T. Hayashi, M. Tanaka, *Org. Lett.* **2003**, *5*, 3349–3352; c) S. Gaillard, J. Bosson, R. S. Ramón, P. Num, A. M. Z. Slawin, S. P. Nolan, *Chem. Eur. J.* **2010**, *16*, 13729–13740.

[12] Z. Lu, J. Han, G. B. Hammond, B. Xu, *Org. Lett.* **2015**, *17*, 4534–4537.

[13] D. Wang, R. Cai, S. Sharma, J. Jirak, S. K. Thummanapelli, N. G. Akhmedov, H. Zhang, X. Liu, J. L. Peterson, X. Shi, *J. Am. Chem. Soc.* **2012**, *134*, 9012–9019.

[14] a) R. S. Paton, F. Maseras, *Org. Lett.* **2009**, *11*, 2237–2240; b) A. S. K. Hashmi, S. Pankajakshan, M. Rudolph, E. Enns, T. Bander, F. Rominger, W. Frey, *Adv. Synth. Catal.* **2009**, *351*, 2855–2875; c) T. Fan, X. Chen, J. Sun, Z. Lin, *Organometallics* **2012**, *31*, 4221–4227; d) J. Jiang, Y. Liu, C. Hou, Y. Li, Z. Luan, C. Zhao, Z. Ke, *Org. Biomol. Chem.* **2016**, *14*, 3558–3563; e) X. Zhang, Z. Geng, *RSC Adv.* **2016**, *6*, 62099–62108; f) B. Herlé, P. M. Holstein, A. M. Echavarren, *ACS Catal.* **2017**, *7*, 3668–3675; g) C. Wang, Q. Cui, Z. Zhang, Z. Yao, S. Wang, Z. Yu, *Chem. Eur. J.* **2019**, *25*, 9821–9826; h) A. A. Ogunlana, Z. Bao, *Chem. Commun.* **2019**, *55*, 11127–11130.

[15] a) M. Jia, M. Bandini, *ACS Catal.* **2015**, *5*, 1638–1652; b) J. Schießl, J. Schulmeister, A. Doppiu, E. Wörner, M. Rudolph, R. Karch, A. S. K. Hashmi, *Adv. Synth. Catal.* **2018**, *360*, 3949–3959; c) A. Zhdanko, M. E. Maier, *ACS Catal.* **2014**, *4*, 2770–2775.

[16] D. Zuccaccia, L. Belpassi, F. Tarantelli, A. Macchioni, *J. Am. Chem. Soc.* **2009**, *131*, 3170–3171.

[17] N. Salvi, L. Belpassi, D. Zuccaccia, F. Tarantelli, A. Macchioni, *J. Organomet. Chem.* **2010**, *695*, 2679–2686.

[18] D. Zuccaccia, L. Belpassi, L. Rocchigiani, F. Tarantelli, A. Macchioni, *Inorg. Chem.* **2010**, *49*, 3080–3082.

[19] G. Ciancaleoni, L. Biasiolo, G. Bistoni, A. Macchioni, F. Tarantelli, D. Zuccaccia, L. Belpassi, *Organometallics* **2013**, *32*, 4444–4447.
[20] D. Sorbelli, J. Segato, A. Del Zotto, L. Belpassi, D. Zuccaccia, P. Belanzoni, *Dalton Trans.* **2021**, *50*, 5154–5160.
[21] a) A. Macchioni, *Chem. Rev.* **2005**, *105*, 2039–2073; b) J. R. Pliego Jr., *Org. Biomol. Chem.* **2021**, *19*, 1900–1914.
[22] Y. Ma, H. Saqib Ali, A. A. Hussein, *Catal. Sci. Technol.* **2022**, *12*, 674–685.
[23] a) A. S. K. Hashmi, J. P. Weyrauch, W. Frey, J. W. Bats, *Org. Lett.* **2004**, *6*, 4391–4394; b) A. Cervantes-Reyes, F. Rominger, M. Rudolph, A. S. K. Hashmi, *Chem. Eur. J.* **2019**, *25*, 11745–11757; c) A. Cervantes-Reyes, F. Rominger, M. Rudolph, A. S. K. Hashmi, *Adv. Synth. Catal.* **2020**, *362*, 2523–2533.
[24] a) C. M. Krauter, A. S. K. Hashmi, M. Pernpointner, *ChemCatChem* **2010**, *2*, 1226–1230; b) P. M. Stein, M. Rudolph, A. S. K. Hashmi, *Adv. Synth. Catal.* **2021**, *363*, 4264–4271.
[25] J. C. Timmerman, B. D. Robertson, R. A. Widenhoefer, *Angew. Chem. Int. Ed.* **2015**, *54*, 2251–2254; *Angew. Chem.* **2015**, *127*, 2279–2282.
[26] A. Couce-Rios, A. Lledós, I. Fernández, G. Ujaque, *ACS Catal.* **2019**, *9*, 848–858.
[27] N. Fey, J. M. Lynam, *WIREs Comput. Mol. Sci.* **2022**, *12*, e1590.
[28] Z. Zhang, S. D. Lee, R. A. Widenhoefer, *J. Am. Chem. Soc.* **2009**, *131*, 5372–5373.
[29] Z. Dong, C.-H. Liu, Y. Wang, M. Lin, Z.-X. Yu, *Angew. Chem. Int. Ed.* **2013**, *52*, 14157–14161; *Angew. Chem.* **2013**, *125*, 14407–14411.
[30] a) A. D. Patil, A. J. Freyer, L. Killmer, P. Offen, B. Carte, A. J. Jurewicz, R. K. Johnson, *Tetrahedron* **1997**, *53*, 5047–5060; b) F. Marion, D. E. Williams, B. O. Patrick, I. Hollander, R. Mallon, S. C. Kim, D. M. Roll, L. Feldberg, R. Van Soest, R. J. Anderson, *Org. Lett.* **2006**, *8*, 321–324; c) S. Panichanun, I. R. C. Bick, *Tetrahedron* **1984**, *40*, 2685–2689.
[31] a) S. J. Pastine, S. Won Youn, D. Sames, *Org. Lett.* **2003**, *5*, 1055–1058; b) Y. Yamamoto, S. Kuwabara, Y. Ando, H. Nagata, H. Nishiyama, K. Itoh, *J. Org. Chem.* **2004**, *69*, 6697–6705; c) H. Yamamoto, I. Sasaki, H. Imagawa, M. Nishizawa, *Org. Lett.* **2007**, *9*, 1399–1402; d) R. S. Menon, M. G. Banwell, *Org. Biomol. Chem.* **2010**, *8*, 5483–5485.
[32] R. G. Epton, W. P. Unsworth, J. M. Lynam, *Organometallics* **2022**, *41*, 497–507.
[33] S. Aikonen, M. Muuronen, T. Wirtanen, S. Heikkinen, J. Musgreave, J. Burés, J. Helaja, *ACS Catal.* **2018**, *8*, 960–967.
[34] M. Kreuzahler, G. Haberhauer, *Angew. Chem. Int. Ed.* **2020**, *59*, 17739–17749; *Angew. Chem.* **2020**, *132*, 17892–17902.
[35] a) M. Kreuzahler, A. Daniels, C. Wölper, G. Haberhauer, *J. Am. Chem. Soc.* **2019**, *141*, 1337–1348; b) M. Kreuzahler, G. Haberhauer, *Angew. Chem. Int. Ed.* **2020**, *59*, 9433–9437; *Angew. Chem.* **2020**, *132*, 9519–9524; c) M. Kreuzahler, G. Haberhauer, *J. Org. Chem.* **2019**, *84*, 8210–8224; d) M. E. de Orbe, M. Zanini, O. Quinonero, A. M. Echavarren, *ACS Catal.* **2019**, *9*, 7817–7822.

Manuscript received: May 17, 2022
Revised manuscript received: July 8, 2022
Version of record online: ■■, ■■

REVIEW

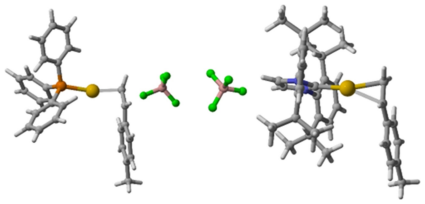

R. G. Epton, Dr. W. P. Unsworth, Dr. J. M. Lynam**